The Astrophysical Journal, 579:337–358, 2002 November 1

NUMERICAL STUDIES OF COSMIC-RAY INJECTION AND ACCELERATION

Hyesung Kang
Department of Earth Sciences, Pusan National University, Pusan 609-735, Korea; kang@uju.es.pusan.ac.kr

T. W. Jones
Department of Astronomy, University of Minnesota, Minneapolis, MN 55455; twj@msi.umn.edu

and

U. D. J. Gieseler
Fachbereich Physik, Universität Siegen, 57068 Siegen, Germany; ug@nesa1.uni-siegen.de
Received 2002 February 22; accepted 2002 July 9

ABSTRACT

A numerical scheme that incorporates a thermal leakage injection model into a combined gasdynamics and cosmic-ray (CR) diffusion-convection code has been developed. The hydro/CR code can follow in a very cost-effective way the evolution of CR-modified planar quasi-parallel shocks by adopting subzone shock tracking and multilevel adaptive mesh refinement techniques. An additional conservative quantity, $S = P_g/\rho^{\gamma_g-1}$, is introduced to follow the adiabatic compression accurately in the precursor region, especially in front of strong, highly modified shocks. The "thermal leakage" injection model is based on the nonlinear interactions of the suprathermal particles with self-generated MHD waves in quasi-parallel shocks. The particle injection is followed numerically by filtering the diffusive flux of suprathermal particles across the shock to the upstream region according to a velocity-dependent transparency function that controls the fraction of leaking particles. This function is determined by a single parameter, ϵ, which should depend on the strength of postshock wave turbulence but is modeled as a constant parameter in our simulations. We have studied CR injection and acceleration efficiencies during the evolution of CR-modified planar shocks for a wide range of initial shock Mach numbers, M_0, assuming a Bohm-like diffusion coefficient. For expected values of ϵ the injection process is very efficient when the subshock is strong, leading to fast and significant modification of the shock structure. As the CR pressure increases, the subshock weakens and the injection rate decreases accordingly so that the subshock does not disappear. Although some fraction of the particles injected early in the evolution continue to be accelerated to ever higher energies, the postshock CR pressure reaches an approximate time-asymptotic value because of a balance between fresh injection/acceleration and advection/diffusion of the CR particles away from the shock. In the strong shock limit of $M_0 \gtrsim 30$, the injection and acceleration processes are largely independent of the initial shock Mach number for a given ϵ, while they are sensitively dependent on M_0 for $M_0 < 30$. We conclude that the injection rates in strong parallel shocks are sufficient to lead to rapid nonlinear modifications to the shock structures and that self-consistent injection and time-dependent simulations are crucial to understanding the nonlinear evolution of CR-modified shocks.

Subject headings: acceleration of particles — cosmic rays — hydrodynamics — methods: numerical

1. INTRODUCTION

Two decades ago it was recognized that cosmic rays (CRs) are probably produced very efficiently via diffusive shock acceleration (DSA) in ubiquitous astrophysical shocks, (for early reviews see, e.g., Drury 1983; Blandford & Eichler 1987; Berezhko & Krymskii 1988). After the initial successes of the simple concept that the particles can gain energy while temporarily trapped in the converging flows around a shock, it was quickly realized that the full DSA treatment requires one to consider the complex nonlinear interactions between energetic particles, resonantly scattering waves, and the underlying plasma (Malkov & Drury 2001). One of the important aspects of those interactions is the injection of suprathermal particles into the CR population at shocks. According to quasi-linear theory as well as plasma simulations of strong quasi-parallel shocks, the streaming motion of superthermal particles against the background plasma can induce wave generation leading to strong downstream MHD waves that scatter particles and inhibit the particles from leaking upstream (e.g., Bell 1978; Quest 1988). Particles in or close to the thermal population are especially restricted in this way. As a consequence only a small fraction of suprathermal particles can swim upstream against the wave-particle interactions in the plasma flow and be injected into the higher energy CR population to be further accelerated via the Fermi process. The injection process and its efficiency control the amplitude of the CR population and hence the degree of shock modification.

Recently, significant progress in understanding this injection process in parallel shocks has been made through self-consistent, analytic, nonlinear calculations by Malkov & Völk (1995) and Malkov (1998). The resulting theory has only one parameter, namely, the intensity of the downstream waves, and that is tightly restricted by both the theory and comparison with hybrid plasma simulations. By adopting Malkov's analytic solution, we have developed a numerical treatment of this injection model and incorporated it into a combined gasdynamics and CR diffusion-convection code (Gieseler, Jones, & Kang 2000). According

to the Gieseler et al. (2000) simulations, the injection process seemed to be self-regulated in such a way that the injection rate reaches and stays at a nearly stable value after quick initial adjustment but well before the CR shock reaches a steady state structure. Gieseler et al. (2000) found about 10^{-3} of incoming thermal particles to be injected into the CRs, roughly independent of Mach numbers. However, owing to severe computational requirements associated with the need to resolve structures down to the physical shock thickness, those simulations were carried out only until the characteristic maximum momentum of $(p_{\max}/m_p c) \sim 1$ was achieved. Since strong shocks were still evolving at the end of the simulations, the time-asymptotic limit could not be estimated for either the CR acceleration efficiency or the CR spectrum.

Unlike ordinary gas shocks, the CR shock is a collisionless structure and includes a wide range of length scales associated not only with the dissipation into "thermal plasma," but also with the nonthermal particle diffusion process. Those are characterized by the so-called diffusion lengths $D_{\rm diff}(p) = \kappa(p)/u$, where $\kappa(p)$ is the spatial diffusion coefficient for CRs of momentum p, and u is the characteristic flow velocity (Kang & Jones 1991). For strong scattering of suprathermal particles $D_{\rm diff}$ may not greatly exceed the physical dissipative, or "gas" shock thickness. Accurate solutions to the CR diffusion-convection equation require a computational grid spacing significantly smaller than $D_{\rm diff}$, typically $\Delta x \sim 0.1 D_{\rm diff}(p)$. On the other hand, for a realistic diffusion transport model with a steeply momentum-dependent diffusion coefficient, the highest energy, relativistic particles have diffusion lengths many orders of magnitude greater than those of the lowest energy particles.

To follow the acceleration of highly relativistic CRs from suprathermal energies, all those scales need to be resolved numerically. However, the diffusion and acceleration of the low-energy particles are important only close to the shock owing to their small diffusion lengths. Elsewhere, they are effectively advected along with the underlying gas flow. At higher energies the needed resolution is less severe, and on scales larger than $\sim D_{\rm diff}(p_{\max})$ the bulk flow and the nonthermal particles decouple, so resolution requirements are controlled by whatever factors are necessary to define the broader flow properties.

Thus, it is necessary to resolve numerically the diffusion length of the particles only around the shock. So in Kang et al. (2001) we first implemented a "shock tracking scheme" (LeVeque & Shyue 1995) to locate the shock position exactly and then refine the grid resolution only around the shock by applying multilevels of refined grids (Berger & LeVeque 1998). The main properties of this code are (1) the shock is tracked as an exact discontinuity; (2) a small region around the shock is refined with multilevel grids; (3) it is very cost-effective in terms of computational memory and time.

In the present contribution, we have studied the CR injection and acceleration during the evolution of modified planar shocks by implementing the numerical method for the thermal leakage injection model of Gieseler et al. (2000) into an enhanced version of the CR/AMR (adaptive mesh refinement) hydrodynamics code, which we name CRASH (Cosmic-Ray Amr SHock) code. With our new CRASH code we were able to calculate the CR injection and acceleration efficiencies with a Bohm-like diffusion coefficient for higher particle energies ($p/m_p c \gg 1$) in shocks over a wide range of initial Mach numbers. In the following section the basic equations solved in the simulations are presented. We describe the thermal leakage injection model and its numerical implementation in our CR transport code in § 3. We then outline our numerical methods in the CR/AMR hydrodynamics code in § 4. In § 5 we present and discuss our simulation results, followed by a summary in § 6. Finally, we discuss some test calculations in the Appendix.

2. BASIC EQUATIONS

We solve the standard gasdynamic equations with CR pressure terms added in the conservative, Eulerian formulation for one-dimensional plane-parallel geometry:

$$\frac{\partial \rho}{\partial t} + \frac{\partial (u\rho)}{\partial x} = 0 \, , \tag{1}$$

$$\frac{\partial (\rho u)}{\partial t} + \frac{\partial (\rho u^2 + P_g + P_c)}{\partial x} = 0 \, , \tag{2}$$

$$\frac{\partial (\rho e_g)}{\partial t} + \frac{\partial (\rho e_g u + P_g u + P_c u)}{\partial x} = -L(x, \, t) \, , \tag{3}$$

where P_g and P_c are the gas and the CR pressure, respectively, $e_g = P_g/\rho(\gamma_g - 1) + u^2/2$ is the total energy density of the gas per unit mass, and the rest of the variables have their usual meanings. The injection energy loss term, $L(x, \, t)$, accounts for the energy of the suprathermal particles injected to the CR component at the subshock. L is nonzero only at the subshock transition, as explained at the end of § 3.2 and in § 4.1. CR inertia is neglected, as usual, in such computations. A basic outline of the computational hydrodynamic scheme and its adaptations for this problem are given in § 4.1.

We do include here one unusual adaptation in the CRASH code that significantly improves treatment of the CR precursor region. In conventional conservative, gasdynamical numerical methods, the thermal energy is calculated by subtracting the kinetic energy from the total gas energy e_g. For highly supersonic flows where the kinetic energy is much larger than the thermal energy, however, the numerical errors in calculating the kinetic gas energy could be much larger than the thermal energy itself. Especially in strong CR-modified shocks where the gas flow is compressed through the precursor but remains highly supersonic, it is difficult to follow this preshock compression accurately. In order to alleviate this difficulty, following the approach first introduced by Ryu et al. (1993), we adopt an additional conservative quantity, the "modified entropy,"

$$S = P_g/\rho^{\gamma_g - 1} \, , \tag{4}$$

related to the gas entropy per unit volume. The modified entropy satisfies the following conservation equation (Ryu et al. 1993):

$$\frac{\partial S}{\partial t} + \frac{\partial (uS)}{\partial x} = 0 \, , \tag{5}$$

which is valid outside the dissipative subshock; i.e., where the gas entropy is conserved. Hence, the modified entropy equation is solved outside the subshock, while the total energy equation is applied across the subshock. As we will discuss below, the injection process depends on the properties of the subshock and so on the precursor compression.

Our new hydro code with the modified entropy equation can accurately follow the adiabatic compression through the precursor and provides a better method to follow the injection process.

The diffusion-convection equation for the pitch angle averaged CR distribution function $f(p,\ x,\ t)$ (e.g., Skilling 1975) is given by

$$\frac{\partial f}{\partial t}+u\frac{\partial f}{\partial x}=\frac{1}{3}\left(\frac{\partial u}{\partial x}\right)p\frac{\partial f}{\partial p}+\frac{\partial}{\partial x}\left[\kappa(x,\ p)\frac{\partial f}{\partial x}\right], \qquad (6)$$

and $\kappa(x,\ p)$ is the diffusion coefficient. For convenience we always express the particle momentum p in units m_pc. As in our previous studies, the function $g(p)=p^4f(p)$ is evolved instead of $f(p)$ and $y=\ln(p)$ is used instead of the momentum variable p for that step. This leads the equation solved to take the form (Kang & Jones 1991; Gieseler et al. 2000)

$$\frac{\partial g}{\partial t}+u\frac{\partial g}{\partial x}=\frac{1}{3}\left(\frac{\partial u}{\partial x}\right)\left(\frac{\partial g}{\partial y}-4g\right)+\frac{\partial}{\partial x}\left[\kappa(x,\ y)\frac{\partial g}{\partial x}\right]. \qquad (7)$$

Our numerical approach to this equation is outlined in § 4.1 with additional details provided in the cited literature.

3. THERMAL LEAKAGE INJECTION MODEL

3.1. *Transparency Function*

In the "thermal leakage" injection model, most of the downstream thermal protons are confined by nonlinear waves, and only particles well into the tail of the Maxwellian distribution can leak upstream across the subshock. Since any escaping particles have to swim against the advection flow downstream, the breadth of the thermal velocity distribution relative the downstream flow velocity in the subshock rest frame is central to the injection problem. In order to model this injection process in Gieseler et al. (2000) we adopted a "transparency function," $\tau_{\rm esc}$, which expresses the probability that suprathermal particles at a given velocity can leak upstream through the magnetic waves, based on nonlinear particle interactions with self-generated waves (Malkov 1998). In this scheme, the transparency function is *approximated* by the functional form

$$\tau_{\rm esc}\left(\epsilon,\ \frac{v}{u_d}\right)=H[\tilde{v}-(1+\epsilon)]\left(1-\frac{u_d}{v}\right)^{-1}\left(1-\frac{1}{\tilde{v}}\right)\times\exp\left\{-[\tilde{v}-(1+\epsilon)]^{-2}\right\}, \qquad (8)$$

which depends on the ratio of particle velocity v to downstream flow velocity in the subshock rest frame $u_d=u_s/r_{\rm sub}$, where u_s and $r_{\rm sub}$ are the subshock velocity with respect to the immediate upstream flow and the subshock compression factor, respectively. Here H is the Heaviside step function. The parameter $\epsilon=B_0/B_\perp$ is defined in Malkov (1998) and measures the ratio of the amplitude of the postshock MHD wave turbulence $B_\perp$ to the general magnetic field aligned with the shock normal B_0. Here $\tilde{v}=\epsilon v/u_d$ is the normalized particle velocity.

The lower right panel of Figure 1 shows the Maxwellian distribution function $g_{\rm M}(p)=f_{\rm M}(p)p^4$ for the subshock Mach number $M_s=100$, and $\tau_{\rm esc}(p)$ as a function of v/u_d for $\epsilon=0.3$ (*solid line*) and $\epsilon=0.2$ (*dashed line*). The function $g_{\rm M}$ is plotted for $\beta=u_s/c=0.01$. The function $\tau_{\rm esc}$ plotted as a function of v/u_d is independent of β. The plot for $\tau_{\rm esc}(p)$ shows that the injection occurs predominantly for the particles with $5u_d<v<20u_d$, where $0<\tau_{\rm esc}(p)<1$. The lower velocity particles with $\tau_{\rm esc}\approx 0$ represent the gas particles, while the higher velocity particles with $\tau_{\rm esc}\approx 1$ represent the CR particles. So the particles are injected over a range of particle momenta rather than a singly chosen injection momentum. Thus, the transparency function eliminates the need to set up the lowest momentum boundary that arbitrarily and abruptly distinguishes thermal plasma and accelerated particles. If one takes a step function (i.e., $\tau_{\rm esc}=0$ for $p<p_{\rm inj}$ and $\tau_{\rm esc}=1$ for $p\geq p_{\rm inj}$) rather than a smooth function for the transparency function, the injection model becomes the same as the earlier injection models where the particles are injected at an injection momentum, $p_{\rm inj}$, which is then the momentum boundary between thermal and CR particles (e.g., Berezhko, Ksenofontov, & Yelshin 1995; Kang & Jones 1995).

The only free parameter of the adopted transparency function is ϵ, and it is rather well constrained, since $0.3\lesssim\epsilon\lesssim 0.4$ is indicated for strong shocks (Malkov & Völk 1998). Due to the exponential cutoff in a thermal velocity distribution, however, the injection rate depends sensitively on the value of ϵ, since the location in the Maxwellian tail distribution where $\partial\tau_{\rm esc}/\partial p\neq 0$ depends on ϵ (see Fig. 1, *lower right panel*). Since the wave generation is relatively less efficient for weak shocks, resulting in larger values of ϵ, this parameter should be dependent on the subshock Mach number. However, since it is not certain precisely how ϵ should vary as the subshock becomes weaker with time, we will keep the value of ϵ constant within each simulation except for a few models where ϵ is changed during the simulation to avoid a numerical problem during initialization. We expect the injection rate would be higher if we let ϵ increase as the subshock weakens, compared with the calculation with a constant value. Although larger values of ϵ naturally lead to higher injection rate and higher acceleration efficiency, as we will show in § 5.1.2, the net enhancement of CR energy would be minimal (a few percent), since the CRs injected earlier are dominant over the fresh particles injected recently at much weaker shocks with a much smaller injection rate. Another degree of freedom in this model is the detailed functional form of the transparency function. The form given by equation (8), which is an approximation of the representation given in Malkov & Völk (1998), behaves like a smoothed step function that selects the range of injection momenta for a given value of ϵ. With a modification in the shape of the transparency function (due to a more accurate approximation), we expect the resulting injection rate may not change significantly, as long as the adopted $\tau_{\rm esc}$ has the characteristics of a smoothed step function and picks the similar momentum range for the injection pool.

3.2. *Numerical Scheme for Injection Model*

In Gieseler et al. (2000) we proposed a new numerical scheme for injection to be used in kinetic equation simulations of DSA. The scheme emulates thermal leakage injection through the transparency function given by equation (8) for particle leakage across a shock discontinuity. The total particle distribution function consists of Maxwellian and CR components ($g=g_{\rm M}+g_{\rm CR}$), and there is no discrete momentum boundary between the two components. In our scheme the Maxwellian distribution, $g_{\rm M}(p,\ x,\ t)$ is calculated from the density and temperature of the local gas at each time step from gasdynamical data, since it cannot be

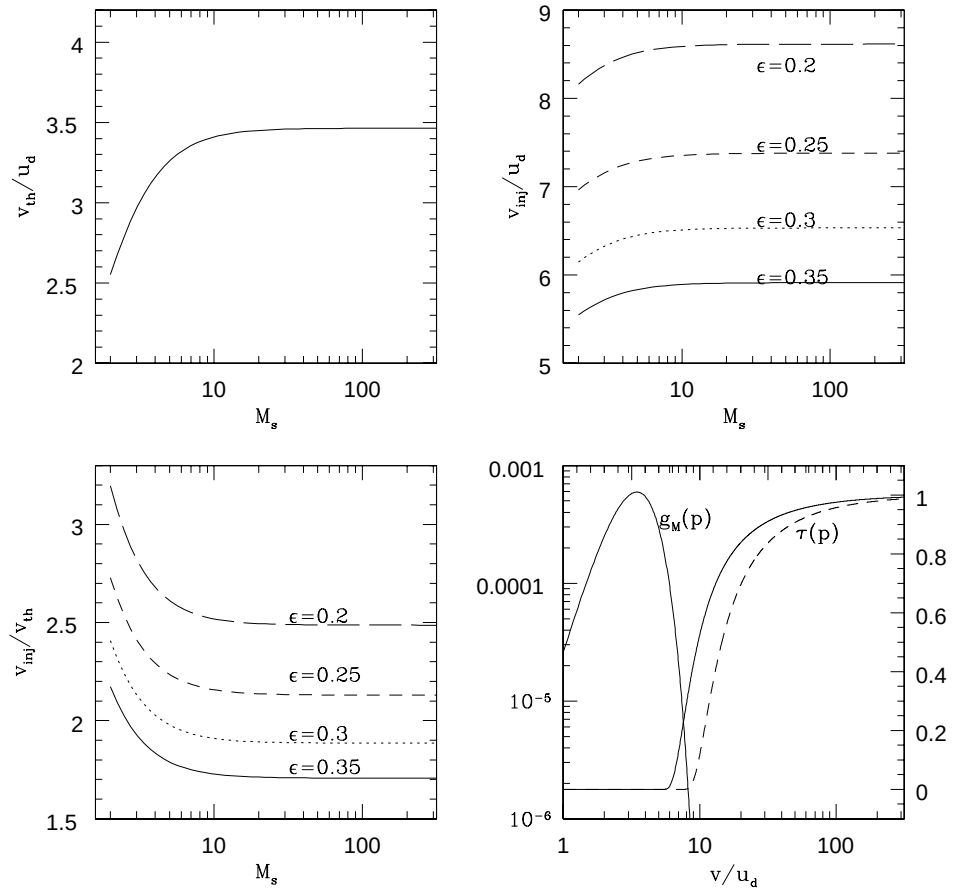

FIG. 1.—Thermal velocity, $v_{\rm th}$, and "effective" injection velocity, $v_{\rm inj}$, both normalized by the downstream flow velocity relative to the subshock, u_d, shown as functions of subshock Mach numbers. The effective injection velocity is also dependent on the inverse wave parameter, ϵ. In the lower left panel, the ratios of $v_{\rm inj}/v_{\rm th}$ are plotted for $\epsilon = 0.2$–0.35. Thermal leakage is faster for smaller $v_{\rm inj}/v_{\rm th}$. In the lower right panel, the thermal distribution function $g_{\rm M}$ of the downstream gas for $M_0 = 100$ shock is plotted against v/u_d, where $u_d = u_s/r_{\rm sub}$, $u_s/c = 0.01$, c is the speed of light, and $r_{\rm sub}$ is the subshock compression ratio. The transparency function, $\tau_{\rm esc}$, for the same shock is also shown for $\epsilon = 0.3$ (*solid line*) and 0.2 (*dashed line*). The axis on the left side is for $\log g_{\rm M}$, while the axis on the right side is for $\tau_{\rm esc}$.

followed by the diffusion-convection equation (6). The suprathermal particles in this "injection pool" should have a significant anisotropic component, so the distribution there cannot be followed by the diffusion-convection equation either. In point of fact, one cannot cleanly demark particles as thermalized and fluid-like or nonthermal and diffusive, yet economical computational schemes exist only in those two limits. That is the very reason we need an injection model as represented here through the transparency function.

We briefly explain how the distribution function is integrated in a way that can implement the thermal leakage process in our CR transport code:

1. The total particle distribution is updated in distinct "advection and diffusion" steps for the momentum bins with $\tau_{\rm esc} > 0$: $g^n \rightarrow \tilde{g}^{n+1}$, where g^n is the value at the previous time step, and $\tilde{g}^{n+1}$ is an intermediate value for g^{n+1}. For thermal particles with $\tau_{\rm esc} = 0$, $g^{n+1} = g_{\rm M}^{n+1}$. Then the CR distribution up to this intermediate step is given by $\tilde{g}_{\rm CR}^{n+1} = \tilde{g}^{n+1} - g_{\rm M}^{n+1}$.

2. The net increase of CR particles, $(\tilde{g}_{\rm CR}^{n+1} - g_{\rm CR}^{n})$, calculated from the diffusion-convection equation (6) should be reduced according to the transparency function in the upstream region. So an additional "leakage" step is applied to the CR distribution function in the upstream region as

$$g_{\rm CR}^{n+1} = g_{\rm CR}^{n} + \tau_{\rm esc}(t)\left(\tilde{g}_{\rm CR}^{n+1} - g_{\rm CR}^{n}\right) . \quad (9)$$

In other words, we first estimate the number of suprathermal particles that cross the shock according to the diffusion-convection equation, and then we allow only some fraction of the combined advective and diffusive fluxes to leak upstream with the probability prescribed by $\tau_{\rm esc}$. Obviously, the CR particles with $\tau_{\rm esc} = 1$ are not affected by the leakage step.

We then need to estimate the gas energy loss rate at the subshock, $L(x,\ t)$, due to particle leakage in order to conserve total energy. Although the injection process is realized numerically via the leakage of suprathermal particles to the upstream region (i.e., diffusion in space), we formulate the energy loss rate due to injection in terms of the particle acceleration in momentum space, because leaking particles experience an adiabatic energy increase upon crossing the subshock. The particle number flux crossing the momentum boundary at p due to the adiabatic change of the momentum through the flow compression/expansion is given by $\tau_{\rm esc}(p)Q(p)$, where $Q(p) = -(4\pi/3)p^3 f(p)(\partial u/\partial x)$, since $\tau_{\rm esc}(p)$ gives the probability for the suprathermal particles to

cross the shock. Then the net change of the particle number density per unit time in the momentum bin bounded by p and $p + dp$ can be written as

$$dN_p = \tau_{\rm esc}(p + dp)Q(p + dp) - \tau_{\rm esc}(p)Q(p) \approx \frac{\partial \tau_{\rm esc}}{\partial p} Q(p)\, dp + \tau_{\rm esc}(p) \frac{\partial Q}{\partial p}\, dp\ . \quad (10)$$

If the transparency function is a step function [i.e., $\partial\tau_{\rm esc}/\partial p = \delta(p_{\rm inj})$], the first term of equation (10) gives the injection rate at $p = p_{\rm inj}$, while the second term represents the acceleration of CRs for $p > p_{\rm inj}$. For a smooth transparency function, the second term contains the acceleration of both CRs and the suprathermal particles, since the momentum boundary between thermal and CR population is soft and $f(p) = f_{\rm CR} + f_M$ for the momenta in the injection pool [i.e., $0 < \tau_{\rm esc}(p) < 1$]. The injection rate due to the second term in equation (10) that corresponds to the acceleration of suprathermal particles should be small because of exponential decrease of f_M in this momentum range. As shown in Figure 1, $\partial\tau_{\rm esc}/\partial p$, for the transparency function adopted here behaves almost like the delta function, and so the first term of equation (10) dominates for the momenta in the injection pool. So we take only the first term to estimate approximately the energy loss rate according to

$$L(x,\ t) \approx -\frac{2\pi}{3} m_p c^2 \frac{\partial u}{\partial x} \int_0^\infty \frac{\partial \tau_{\rm esc}(p,\ t)}{\partial p} p^5 f(p,\ x,\ t)\, dp\ , \quad (11)$$

where we have used the nonrelativistic approximation for the kinetic energy of injected particles, $\frac{1}{2} m_p c^2 p^2$. We remind the reader that p is expressed in units of $m_p c$. The term $L(x,\ t)\Delta t$ is then subtracted from the gas thermal energy in the immediate postshock region, and only there. No matching term is necessary in updating the CRs, since L is introduced explicitly to account for evolution of $f(x,\ p,\ t)$ in the "injection pool," where f is in transition between thermal and nonthermal forms. Since the fraction of injected particles is very small, the energy exchanged through L is, in any case, small so that it has little direct influence on the flow.

Since the diffusive flux of particles depends on the particle diffusion length, the CR injection rate numerically realized in our scheme depends on the ratio of $D_{\rm diff}(p_{\rm inj})/\Delta x$ at the finest grid. However, the numerical results seem to be converged at a spatial resolution of $\Delta x \sim D_{\rm diff}(p_{\rm inj})$.

3.3. *Dependence of Injection Rate on the Subshock Mach Number*

As we show below, the ensuing injection rate based on our thermal leakage model depends largely on the subshock Mach number, M_s, and the inverse wave-amplitude parameter, ϵ, because the transparency filter is a function of $\tilde{v} = \epsilon v/u_d$. Here we explore the consequences of this dependence. The thermal peak velocity of the Maxwellian distribution of the immediate postshock gas relative to the mean flow is defined as $v_{\rm th} = 2(k_{\rm B} T_2/m_p)^{1/2}$, where T_2 is the postshock temperature, $k_{\rm B}$ is the Boltzmann constant, and m_p is the proton mass. The mean molecular weight is assumed to be 1 in this consideration and also in our numerical calculations. The ratio of $v_{\rm th}/u_d$ is then determined only by M_s as follows:

$$\frac{v_{\rm th}}{u_d} = \sqrt{\frac{12}{5}\frac{(5M_s^2 - 1)}{(M_s^2 + 3)}}\ , \quad (12)$$

where M_s is the subshock Mach number and we assume $\gamma_g = 5/3$. Since the injected particle flux is approximately proportional to $(\partial\tau_{\rm esc}/\partial p) f(p) p^3\, dp$ (see eq. [11]), we define the "injection velocity" $v_{\rm inj}$ as

$$v_{\rm inj} = \frac{\int_0^\infty v(\partial\tau_{\rm esc}/\partial p) f_{\rm M}(p) p^3\, dp}{\int_0^\infty (\partial\tau_{\rm esc}/\partial p) f_{\rm M}(p) p^3\, dp}\ , \quad (13)$$

where $f_{\rm M}$ is the Maxwellian velocity distribution of the immediate postshock gas. One can easily show that the ratio of $v_{\rm inj}/u_d$ is a function of M_s and ϵ only (see Fig. 1). Since in the model used here the rate of particle injection into the Fermi process is proportional to the convolution of $\partial\tau_{\rm esc}/\partial p$ with the Maxwellian tail distribution, the injection rate is determined mainly by the ratio of $v_{\rm inj}/v_{\rm th}$, rather than the velocities themselves. This ratio depends on only M_s and ϵ. We plot the values of $v_{\rm inj}/v_{\rm th}$ in Figure 1 for $\epsilon = 0.2$–0.35. For strong shocks $M_s \gtrsim 10$ this ratio becomes independent of M_s, while it increases for smaller M_s. To illustrate, for $\epsilon = 0.3$, $v_{\rm inj}/v_{\rm th} = 1.87$ for $M_s \gtrsim 10$, while $v_{\rm inj}/v_{\rm th} \to 2.4$ as $M_s \to 2$. Thus, the injection rate becomes independent of the subshock Mach number for strong shocks. Larger values of $v_{\rm inj}/v_{\rm th}$ for smaller M_s means that the injection process is less efficient for weak shocks. This ratio is also larger for smaller ϵ, since the leakage is prohibited by stronger wave fields. Thus, injection is more strongly inhibited by smaller ϵ (stronger waves).

Since the injected particles are nonrelativistic, the ratio $v_{\rm inj}/v_{\rm th}$, is, in fact, the same as the parameter $c_1 = p_{\rm inj}/p_{\rm th}$ defined as a constant injection parameter in an earlier version of a thermal leakage model by Kang & Jones (1995) where values in the similar ranges (i.e., $c_1 = 1.9$–1.95) were adopted.

As shown above, in a "thermal leakage" injection model where the leakage probability is determined by the ratio of the particle velocity to the advection velocity of the downstream flow relative to the subshock, we can expect the following: (1) the injection rate becomes independent of the subshock Mach number for $M_s \gtrsim 10$; (2) the injection is less efficient for weaker shocks ($M_s < 10$) compared to stronger shocks; (3) in the time evolution of a CR-modified shock the injection rate decreases as the subshock weakens by way of precursor compression.

4. NUMERICAL METHODS AND MODEL PARAMETERS

4.1. *CRASH: A CR/AMR Hydrodynamics Code with Modified Entropy*

Equations (1)–(3) and (5) are solved in two steps on an Eulerian grid: a gasdynamic step without CR terms followed by a CR-dynamic step, as outlined below. Then equation (7) is solved in two steps to update the CR distribution and allow for injection at shocks. The advection term of equation (7) is solved by the wave-propagation method, as for the gasdynamic variables, except that only the entropy wave applies. Then the diffusion term is solved by the semi-

implicit Crank-Nicholson scheme, as described in Kang & Jones (1991).

A full description of the combined gasdynamic/CR algorithm without equation (5) can be found in Kang et al. (2001). We refer readers to that work for most details and a discussion of various algorithm tests. Since we introduce two new features in the present work, namely, an improved treatment of the shock precursor and our new "thermal leakage injection" model, we briefly outline the basic scheme here. Some further, relevant code tests are described briefly in the Appendix.

In the gasdynamic step, the hydrodynamic conservation equations are solved by the explicit, LeVeque-Shyue Riemann-solver-based *wave-propagation* algorithm, temporarily ignoring the CR terms in equations (2) and (3). A nonlinear Riemann problem is solved at each interface between grid zones, and the wave solutions are used directly to update the mean dynamic variables in each zone. In regular zones not including a detected subshock the gas pressure is updated from the modified entropy as $P_g = S\rho^{\gamma_g - 1}$, where S is updated by equation (5) outside the gas shock (subshock). Updating the gas energy from equation (5) instead of equation (3) minimizes errors introduced to the gas pressure due to dominant kinetic energy or P_c gradients in the CR shock precursor. For regular zones including a detected subshock, gas pressure is computed in the more conventional manner from the updated internal energy found by equation (3). The latter is found by subtracting the kinetic energy estimated from equations (1) and (2) from the updated total energy [omitting the $\partial(P_c u)/\partial x$ term across the subshock jump, since by construction the diffusive CRs interact with the gas only over distances exceeding the physical shock thickness].

The employed shock tracking method locates the exact position of the shock within a regular grid zone using the shock speed obtained from the nonlinear Riemann solver and then adds a new zone boundary there. This subdivides a uniform zone of the underlying regular grid into two subzones. In the next time step, this zone boundary (shock front) is moved to a new location using the Riemann solutions at the current shock location, and the waves are propagated onto the new set of grid zones (LeVeque & Shyue 1995). Since the new grid locates the shock precisely at an irregular zone boundary, the shock remains as an exact discontinuity without smearing. The jump conditions across the discontinuous subshock are realized exactly, because the wave solutions from the nonlinear Riemann solver (i.e., speeds of waves and jumps associated with three wave modes) are used directly to update the dynamic variables in each zone. Physically, the shock is not a discontinuity, of course, but a relatively thin layer in which entropy is generated. Since CR shocks are collisionless, this region is difficult to define precisely. Nonetheless, a basic concept behind DSA theory is that we can identify this region and that it is thinner than the interaction scale for even the lowest energy CRs, given roughly by $D_{\rm diff}(p_{\rm inj})$. The need to satisfy this constraint is the main driver for incorporating the shock tracking scheme into the CRASH code, since it minimizes the number of grid zones containing the subshock.

In the CR-dynamic step, $\partial P_c/\partial x$ terms are added to the gas momentum conservation equation (2). The gas total energy, e_g is updated by adding the new, CR-corrected, kinetic energy to the thermal energy. At the subshock (only) the gas energy must also be reduced according to the term L in equation (11) to account for energy removed from the thermal population as particles are converted into CRs (i.e., as they are injected). The quantity L represents the energy per unit volume per unit time transferred from gas to CRs in the immediate postshock region. Physically this should occur over a distance corresponding to the scattering lengths of injected particles, or roughly $D_{\rm diff}(p_{\rm inj})$. In practice we spread this exchange over three postshock zones of the finest refined grid (see the following paragraph), which is slightly broader but reduces numerical difficulties encountered if the energy is extracted too abruptly. This step is analogous to the inclusion of radiative energy losses in shocks, except that here the energy extraction is limited to very close postshock distances.

In order to follow accurately the evolution of a CR-modified shock, it is necessary to resolve the precursor structure immediately upstream of the subshock and, at the same time, to solve correctly the diffusion of the low-energy particles near the injection pool. Both of those have scales slightly greater than $D_{\rm diff}(p_{\rm inj})$. While the full extent of the precursor increases with the diffusion length of the maximum accelerated CR momentum, the dominant scale length of the precursor as determined by the gas pressure distribution is similar to an averaged diffusion length of the particle populations with the greatest contribution to the CR pressure. As a result of these complications, a large dynamic range of resolved scales from the shock thickness to the precursor scale is required for CR shock simulations. To solve this problem generally, in order to allow eventually for arbitrary and self-consistent diffusion models, we have successfully combined a powerful "adaptive mesh refinement" technique (Berger & LeVeque 1998) and aforementioned "shock tracking" technique and implemented them into a hydro/CR code based on the wave-propagation method (Kang et al. 2001). The AMR technique allows us to "zoom in" inside the precursor structure using a hierarchy of small, refined grid levels applied around the subshock. The shock tracking technique follows hydrodynamic shocks within regular zones and maintains them as true discontinuities, thus allowing us to refine the region around the gas subshock at an arbitrarily fine level. The result is an enormous savings in both computational time and data storage over what would be required to solve the problem using more traditional methods on a single fine grid.

Figure 2 shows the evolution of the gas density within the refinement region on the $l_g = 1,\ 3,\ 5,\ 7$ level grids for a Mach 100 shock (see § 4.4 for detailed model parameters). There are 200 zones in each refined grid level and 2×10^4 zones in the base grid. The size of the refinement region is reduced by a factor of 2 between adjacent grid levels, so the spatial resolution is refined by the same factor. Figure 2 demonstrates that the refinement region shrinks by a factor of 2^2 for $\Delta l_g = 2$ and moves along with the shock. We also plotted the values at 200 zones with filled circles at $\tilde{t} = 20$ in order to demonstrate that the subshock is resolved as a discontinuous jump (see § 4.3 for the definition of time variable $\tilde{t}$).

4.2. *Bohm Diffusion Model*

The spatial diffusion coefficient can be expressed in terms of a mean scattering length λ as $\kappa(x,\ p) = \frac{1}{3}\lambda v$, where v is the particle velocity. The scattering length, λ, and thus $\kappa(x,\ p)$ should be, in principle, determined by the intensity

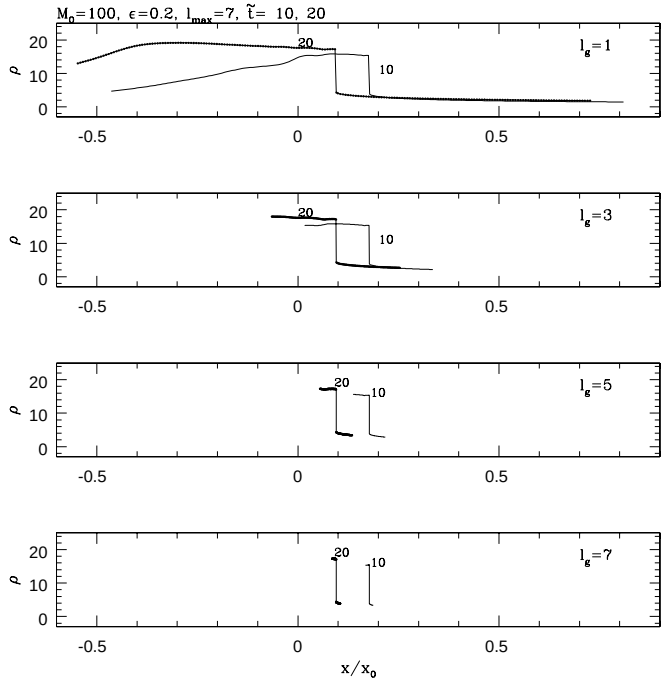

FIG. 2.—Density profile in the refinement region around the shock for $M_0 = 100$ and $\epsilon = 0.2$ model at $\tilde{t} = 10$ and 20 at the grid level $l_g = 1$, 3, 5, and 7. There are 200 zones at each grid level, which are shown as filled points at $\tilde{t} = 20$ curves.

of resonantly interacting Alfvén waves. For example, the Bohm diffusion model represents a saturated wave spectrum and gives the minimum diffusion coefficient as $\kappa_B = 1/3 r_g v$, when the particles scatter within one gyration radius (r_g) due to completely random scatterings off the self-generated waves. This gives $\kappa_B \propto p^2/(p^2+1)^{1/2}$. We consider here only the proton CR component. As stated before, we express particle momenta in units of $m_p c$. In order to model amplification of self-generated turbulent waves due to compression of the perpendicular component of the magnetic field, the spatial dependence of the diffusion is modeled as

$$\kappa(x,\ p) = \kappa(p)\left[\frac{\rho_0}{\rho(x)}\right] , \qquad (14)$$

where ρ_0 is the upstream gas density. This form is also required to prevent the acoustic instability of the precursor (Drury & Falle 1986; Kang, Jones, & Ryu 1992).

Here we define the acceleration timescale for a particle to reach momentum p (e.g., Drury 1983) as

$$\tau_{\rm acc}(p) = \frac{p}{\langle dp/dt\rangle} = \frac{3}{u_1 - u_2}\left(\frac{\kappa_1}{u_1} + \frac{\kappa_2}{u_2}\right) \approx \frac{8}{u_s^2}\kappa_B(p) , \qquad (15)$$

where subscripts 1 and 2 designate the upstream and downstream conditions, respectively. The last expression is approximated for the velocity jump for a strong gas shock. For the Bohm diffusion coefficient the acceleration time of relativistic particles increases linearly with the momentum, so both the required simulation time and the simulation box size increase linearly with the highest momentum to be accelerated. Hence, it becomes extremely costly to extend the CR spectrum to $p_{\rm max} \gg 1$ even with our very efficient CRASH code.

4.3. *Model Parameters*

A CR-modified shock has more complex structure than a discontinuous jump. A precursor develops and the subshock weakens as the flow is modified by the CR pressure. We follow Berezhko & Ellison (1999) to denote the values at the far upstream as u_0 and ρ_0, the values immediately upstream of the subshock as u_1 and ρ_1, and the values immediately downstream of the subshock as u_2 and ρ_2. We use u_s as the subshock velocity relative to the immediate pre-subshock flow and u_d as the immediate downstream flow velocity in the rest frame of the subshock. The gas flow is compressed adiabatically in the precursor, so the gas pressure immediately upstream of the subshock is given by $P_{g,1} = P_{g,0}(\rho_1/\rho_0)^{\gamma_g}$.

The evolution of the CR-modified shock depends on four parameters: the gas adiabatic index, γ_g; the *initial* Mach number of the gas shock, $M_0 = |u_0|/c_{s,0}$; $\beta = u_o/c$; and the diffusion coefficient, $\kappa(p)$. Here u_0 is the upstream flow velocity relative to the initial, unmodified shock, and u_o is the velocity normalization constant, which is set to be $|u_0|$. We assume $\gamma_g = 5/3$. For all simulations we present here $u_0 = 3000$ km s^{-1}, so $\beta = 10^{-2}$. We assume a Bohm-like diffusion coefficient, $\kappa_B = \kappa_0 p^2/(p^2+1)^{1/2}$. The length and the time variables scale with κ_0 through the diffusion length and time defined as $r_0 = \kappa_0/u_0$ and $t_0 = \kappa_0/u_0^2$, respectively. Thus, we do not need to choose a specific value for κ_0, as long as we adopt r_0 and t_0 as normalization constants for length and timescales, respectively.

We consider a wide range of initial Mach numbers, $M_0 = 2$–200 for the *initial* shock jump by adjusting the initial preshock gas pressure by

$$P_{g,0} = 0.75/(1.25M_0^2 - 0.25) . \qquad (16)$$

The far upstream density and flow velocity are, in code units, fixed at $\rho_0 = 1$, $u_0 = -1$. Thus, the preshock gas is colder for stronger shocks, while the gas density and the shock velocity are the same for all models. Then the initial jump conditions for downstream region in the rest frame of the shock are given as $\rho_2 = r$, $u_2 = -1/r$, $P_{g,2} = 0.75$ in downstream region, where the compression ratio is $r = 4M_0^2/(M_0^2+3)$. Since the subshock velocity changes as the subshock weakens in response to growing upstream CR pressure, the subshock drifts in the initial shock rest frame. In order to keep the subshock close to the center of the simulation box a small velocity shift ($u_{\rm shift}$), which is experimentally determined, is added occasionally to the rest frame of the initial shock. There are no preexisting CRs in the simulated flows, so the CRs are introduced to the system at the shock via thermal leakage as the system evolves.

Although the theoretically preferred values of ϵ lie between 0.3 and 0.4 for strong shocks (Malkov 1998), such values lead to very efficient initial injection for shocks of $M_0 \gtrsim 100$. Efficient injection at the start of the simulation results in the rapid surges of P_c and the precursor at the early stage, which, in fact, are too fast for the code to follow accurately. During this early development the gradients in the precursor are extremely steep. Consequently, the flow structure on the base grid, which is calculated from the average of $2^{l_{\rm max}}$ zones of the finest grid, develops large discrete jumps. The Riemann solver for such flows can fail to converge. For $\epsilon = 0.25$–0.3 we can use up to $l_{\rm max} = 5$ levels of refined grids for $M_0 \leq 100$ shocks without failures of the Riemann solver. For $\epsilon = 0.17$–0.2, $l_{\rm max} = 7$ can be used for

$M_0 \leq 200$ shocks. So we consider two sets of models depending on the injection rate, that is, models with $\epsilon = 0.25$–0.3 and models with $\epsilon = 0.17$–0.2. While these parameter values were applied for practical reasons, the thermal leakage is expected to be more difficult in oblique shocks, so these runs can offer some insights into the importance of that effect.

For the injection models with $\epsilon = 0.25$–0.3, the simulations were carried out on a base grid with $\Delta x_0 = 3.2 \times 10^{-3}$ using $l_{\max} = 5$ additional grid levels, so $\Delta x_5 = 10^{-4}$ on the finest grid. Here spatial resolutions are given in units of r_o. The simulated space is $x = [-12.8,\ 12.8]$, and $N = 8000$ zones are used on the base grid. We have repeated one of the models ($M_0 = 30$ case) with $l_{\max} = 4$ and found that the numerical results are well converged within 1% in terms of CR pressure at this spatial resolution. The number of refined zones around the shock is $N_{\rm rf} = 200$ on the base grid, and so there are $2N_{\rm rf} = 400$ zones on each refined level. The length of the refined region at the base grid is 0.64, so 1/40 of the entire simulated space on the base grid is refined. In these cases we integrate the simulation until $\tilde{t} \equiv t/t_0 = 20$ so that the maximum momentum achieved by the end of simulation is on the order of $p_{\max} \sim 4$, above which the CR distribution function decreases exponentially.

For the injection models with $\epsilon = 0.17$–0.2, the base grid spacing is $\Delta x_0 = 1.28 \times 10^{-2}$ with $l_{\max} = 7$, so $\Delta x_7 = 10^{-4}$ on the finest grid. The simulated space is $x = [-128.0,\ 128.0]$, and $N = 20,000$ zones are used at the base grid. For these models $N_{\rm rf} = 100$ on the base grid and $2N_{\rm rf} = 200$ at each refined level. The length of the refined region at the base grid is 1.28, so only 1/200 of the entire simulated space on the base grid is refined. We integrate these injection models until $\tilde{t} = 100$–300. For all models we use 230 logarithmic momentum zones in the interval $\log(p/m_p c) = [\log p_0,\ \log p_1] = [-3.0,\ +3.0]$.

Gasdynamic variables are assumed to be continuous at both left and right boundaries of the simulation box. For the CR distribution function a continuous boundary is assumed for the advection step, and a no-flux boundary condition is adopted for the spatial diffusion step. Either below p_0 or above p_1, $g(p) = 0$ is assumed. For clarity we distinguish here between the highest momentum included in the simulations p_1 and the value of the momentum $p_{\max}$ characterizing the effective upper cutoff in the actual distribution, $g(p)$. In practical terms, there is generally a clear momentum above which $g(p)$ drops sharply so that we identify as $p_{\max}$. The maximum momentum $p_{\max}$ will generally evolve toward p_1, but in all the simulations reported here remains well below it at the terminal time.

4.4. *Injection and Acceleration Efficiencies*

The fraction of particles that have been swept through the shock after the time t and then injected into the CR distribution is estimated by

$$\xi(t) = \frac{\int dx \int 4\pi f_{\rm CR}(p,\ x,\ t) p^2\, dp}{\int n_0 u_0'(t')\, dt'} , \tag{17}$$

where $f_{\rm CR}$ is the CR distribution function, n_0 is the particle number density, and $u_0'(t)$ is the instantaneous shock velocity relative to the far upstream flow. As the CR pressure becomes dominant for strongly CR mediated shocks, the effective adiabatic index of the flow becomes smaller than 5/3. This combines with other factors discussed below that allow the total shock compression to increase and causes the subshock to slow down with respect to the upstream gas. So the instantaneous shock velocity decreases as the CR pressure increases. One should also note that $\xi(t)$ represents a "moving time-averaged" injection efficiency rather than a current instantaneous value.

As a measure of acceleration efficiency, we define the "CR energy ratio," namely, the ratio of the total CR energy within the simulation box to the kinetic energy in the *initial shock rest frame* that has entered the simulation box from far upstream,

$$\Phi(t) = \frac{\int dx E_{\rm CR}(x,\ t)}{0.5\rho_0 |u_0|^3 t} . \tag{18}$$

The total energy in the simulation box is conserved in the initial shock rest frame, since the total energy flux entering the simulation from far upstream, $0.5\rho_0 u_0^3 + \gamma_g P_{g,0} u_0/(\gamma_g - 1)$, is balanced by the same flux exiting the grid far downstream. We intentionally placed the boundaries well away from the shock to avoid boundary issues. Since our shock models have the same upstream density and velocity but different gas pressure depending on M_0, we use the kinetic energy flux rather than the total energy flux to normalize the "CR energy ratio." For strong shocks the total energy flux becomes the same as the kinetic energy flux.

Since the shock slows down due to nonlinear modification, the kinetic energy flux in the instantaneous shock rest frame also decreases. So we also calculate the ratio of the total CR energy in the simulation box to the kinetic energy defined in the *instantaneous shock frame* that has entered the shock from far upstream,

$$\Phi'(t) = \frac{\int dx E_{\rm CR}(x,\ t)}{\int 0.5\rho_0 u_0'(t)^3\, dt} . \tag{19}$$

5. SIMULATION RESULTS

5.1. *Models with* $\epsilon = 0.25$–0.3

5.1.1. *Shock Structure Modification*

Figures 3 and 4 show time evolution of the CR-modified shock structure for $M_0 = 5$ and $M_0 = 30$ shocks, respectively, with $\epsilon = 0.3$. As CRs are injected and accelerated, the CR pressure increases, the precursor grows, and the subshock slows down and weakens. Nonlinear modification to the shock structure is much stronger, and the subshock drift is greater for higher Mach number models. At the simulation ends the subshock drifts to the left with $u_{\rm drift} \approx -0.14$ for the $M_0 = 30$ shock and with $u_{\rm drift} \approx -0.038$ for the $M_0 = 5$ shock. Since the initial simulation frame was set up with the $u_{\rm shift} = 0.01$ relative to the initial shock rest frame, the subshock drifts in the initial shock rest frame with $u = u_{\rm drift} - 0.01$. Thus, for strong shocks the subshock velocity relative to far upstream flow becomes $u_0' \sim 0.85$ instead of $|u_0| = 1$, approximately independent of M_0. For low Mach number shocks, however, this velocity difference is smaller and increases with M_0 (see also Fig. 12 below).

Owing to strong injection, the CR pressure increases and the modification to the flow structure proceeds very quickly, before $\tilde{t} \lesssim 0.1$. After the initial quick adjustment, the CR pressure at the shock reaches *approximate* time-asymptotic values when the fresh injection and acceleration are bal-

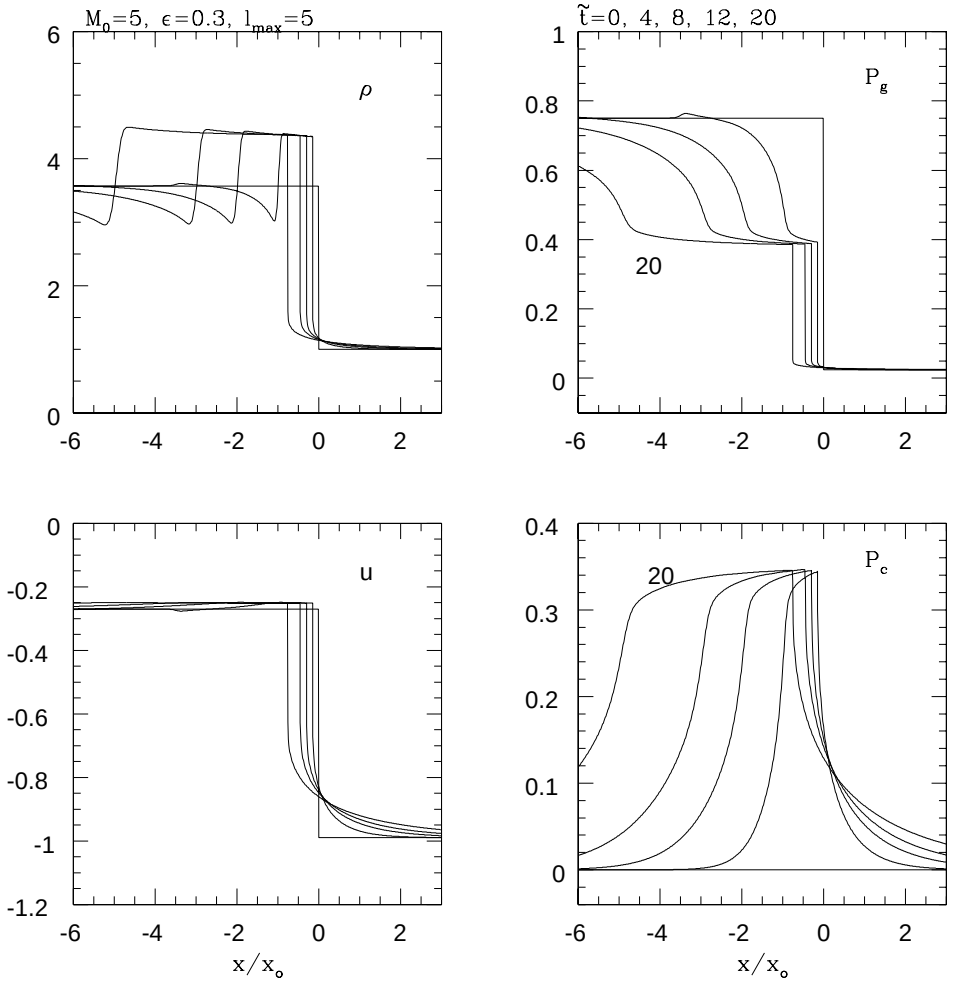

FIG. 3.—Time evolution of the $M_0 = 5$ shock structure with $\epsilon = 0.3$ and $l_{\max} = 5$ refined grid levels. Gas density, pressure, flow velocity, and CR pressure are shown at $t/t_0 = 0, 4, 8, 12$, and 20. The right-facing shock drifts to the left, so the rightmost transitions correspond to the earliest time $t = 0$.

anced with advection and spreading of high-energy particles due to strong diffusion. This balance seems to occur earlier in time for larger values of ϵ for models of a given Mach number (see also Fig. 5 below). For a given value of ϵ, it occurs gradually earlier with increasing initial Mach number but at a similar time in the strong shock limit. We will show below that the time-asymptotic values of P_c are related to the subshock evolution, as well. After $P_{c,2}$ becomes *quasi-steady*, the overall shock structure evolves approximately in a *self-similar* way, as shown in Figures 3–4. This behavior can be understood from the fact that $P_{c,2}$ at the shock stays constant, and the characteristic scale length of P_c and precursor scale length increase linearly with time, since the diffusion length of the highest momentum, $D_{\rm diff}(p_{\max}) \propto t$ for $p_{\max} \gg 1$ and the advection length also scales with time.

The evolution of the density distribution in Figure 4 includes the formation of the postshock "density spike" noted in several previous time-dependent studies (e.g., Jones & Kang 1990). The density spike forms because the weakening of the subshock lags behind formation of the precursor during initial shock modification. For strong shocks this can produce a substantial, temporary "overshoot" in the total compression (see also Fig. 9). That feature eventually detaches from the steady shock and is carried downstream from it.

Evolution of subshock and precursor properties can be seen in Figure 5, where the subshock velocity u_s and Mach number M_s, as well as the pre-subshock gas density ρ_1/ρ_0 and the immediate postshock gas density ρ_2/ρ_0, are plotted against time for the models of $M_0 = 2$–30 and $\epsilon = 0.3$. As mentioned before, the modification to the flow structure occurs mostly before $\tilde{t} \lesssim 0.1$, and so the subshock velocity decreases and the precursor compression increases at the same time. After $\tilde{t} > 0.1$, the subshock Mach number remains nearly constant at $M_s \sim 2$–3 for these shock models, and the subshock persists. Thus, a completely smooth transition never develops. The ratio ρ_2/ρ_0 is greater for higher Mach number shocks and, in fact, follows roughly $M_0^{0.6}$ scaling relation (see § 5.3 for further discussion). In our simulations, the compression continues to grow slowly with time, especially for strong shocks, even after the overall shock structure measured from far upstream through the subshock appears mostly to have reached a "quasi steady state."

Obviously the compression factor is much higher than what is expected in a *steady-state*, energy-conserving shock jump for relativistic gas (i.e., $\rho_2/\rho_0 = 7$ with $\gamma_c = 4/3$). Similar results to ours have been found previously in spherically expanding CR-dominated shocks (Berezhko et al. 1995) and in steady state planar shocks with strongly momentum-dependent diffusion when provision is made for energy

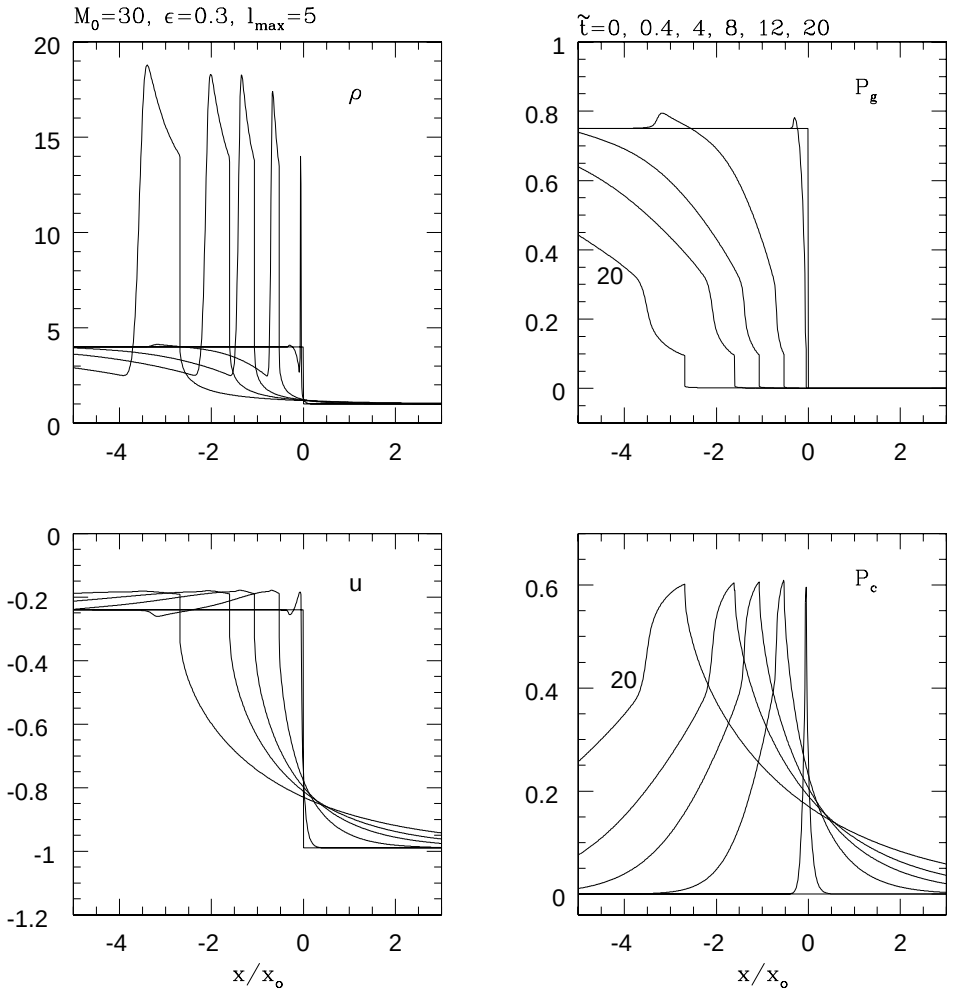

FIG. 4.—Same as Fig. 3, but for time evolution of the $M_0 = 30$ shock structure

losses carried by escaping momentum particles (Malkov 1997; Berezhko & Ellison 1999; Malkov & Drury 2001). While our shocks are not yet truly steady, they have all evolved well past the transient stage associated with the density spike mentioned above. It is very unlikely that the density jumps across our simulated shocks would decrease were they allowed to evolve over much longer times. As noted, compression appears still to be increasing. On the other hand, the spatial and momentum boundaries in our simulations are such that energy losses for the entire system can be ignored, so they might be considered to be conservative.

The key feature in common to the CR shock solutions with nontransient large density jumps is that they all involve significant energy transport away from the transition itself. Drury, Völk, & Berezhko (1995) pointed out that subshock smoothing in spherical systems was inhibited by the fact that CRs diffuse into an ever-increasing volume, thus extracting energy from the shock itself. Steady planar shocks with either a spatial or a momentum "escape" boundary that allows significant energy to leave the shock structure encounter the same effect. Once the momentum distributions in our CR populations near the shock evolved so that $p_{\max} \sim p_1$, they would be influenced by similar "escape" losses. In the meantime they appear to be evolving toward properties that are consistent with those losses. At the "intermediate ages" we see in our shock evolutionary histories, energy is not leaving the system but is being transported out of the region of the subshock by diffusion of the highest energy CRs. The quasi-steady structure is growing in a self-similar manner, in fact, reflecting the linear increase in $D_{\rm diff}(p_{\max})$ with time. Since advection extends the downstream region in a similar way, the immediate postshock properties can remain essentially constant even while the global structure continues to grow in phase space.

Regardless of the quasi-steadiness of the postshock CR pressure and the self- similarity of the flow structure, the CR distribution function continues to become harder and extends to ever higher momenta until scattering becomes too weak to contain the particles. Thus, the adiabatic index of the CRs, $\gamma_c = 1 + P_c/E_c$, decreases with time at the shock and tends toward $4/3$ as the CR pressure and energy become dominated by relativistic particles. This evolution in γ_c is more dramatic away from the subshock and especially upstream, since spatial diffusion is biased toward more energetic particles. This secular evolution of γ_c affects the precursor compression and causes the subshock properties to evolve slowly, especially for strong shocks, as can be seen in Figure 5. Although we adopted the modified entropy equation to follow the precursor adiabatic compression accurately, the subshock properties are not numerically steady but somewhat noisy. This unsteady behavior of the subshock seems to be due to the CR pressure gradient,

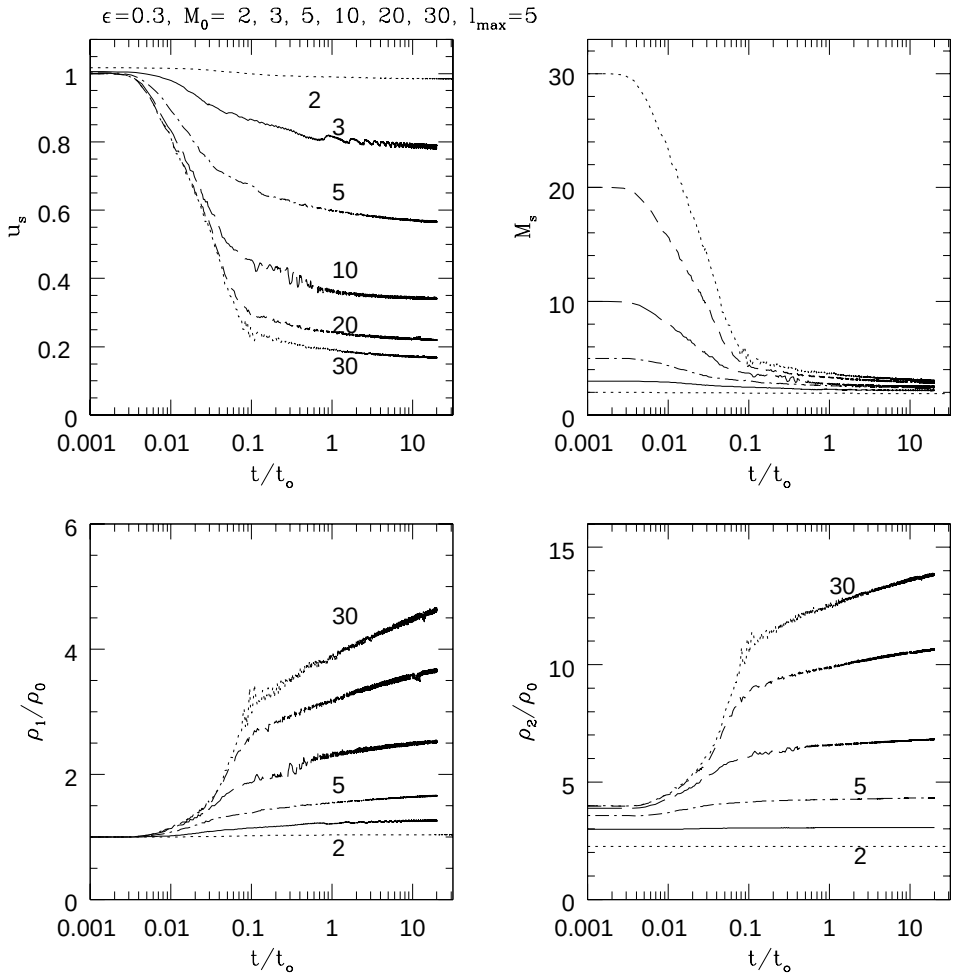

FIG. 5.—Time evolution of subshock velocity u_s, subshock Mach number M_s, preshock density ρ_1/ρ_0, and postshock density ρ_2/ρ_0 are shown for $M_0 = 2$–30 and $\epsilon = 0.3$.

$\partial P_c/\partial x$, which is separately added to the momentum conservation equation. Within the precursor this pressure force is large and compresses the gas adiabatically, so it determines the position and the properties of the subshock. Thus, inside the precursor the accuracy in calculation of P_c distribution would control the subshock calculation rather than the accuracy in calculation of the gas adiabatic compression. If one used a conventional code with the total energy equation alone, these quantities would be much noisier than what is seen in Figure 5.

5.1.2. *Injection and Acceleration Efficiencies*

Figure 6 shows how the CR energy ratio, Φ, the CR pressure at the shock normalized to the far upstream ram pressure in the instantaneous shock frame, $P_{c,2}/\rho_0 u_0'(t)^2$, and the "time-averaged" injection efficiencies, ξ, evolve for shocks with different Mach numbers when $\epsilon = 0.3$ (*left three panels*) or $\epsilon = 0.25$ (*right three panels*) is adopted. As mentioned in the previous section, for all Mach numbers the postshock P_c increases until a balance between injection/acceleration and advection/diffusion of CRs is achieved, and then stays at a steady value afterward. The time-asymptotic value of the CR pressure becomes $P_{c,2}/\rho_0 u_0'(t)^2 \sim 0.8$ for $M_0 = 30$ with $\epsilon = 0.3$. As seen in the previous section, the subshock slows down, and the subshock velocity relative to the far upstream flow becomes $u_0' \sim 0.85|u_0|$ for $M_0 = 30$. Since the subshock has reached a "quasi-steady state" in our simulations, we can apply the mass and momentum flux conservation in the subshock rest frame as

$$\rho_0 u_0' = \rho_1 u_s = \rho_2 u_d \ , \tag{20}$$

$$\rho_2 u_d^2 + P_{g,2} + P_{c,2} = \rho_0 u_0'^2 + P_{g,0} \ . \tag{21}$$

The postshock gas pressure is given by the jump condition, $P_{g,2} = (1.25M_s^2 - 0.25)P_{g,1}$, so it can be approximated as $P_{g,2} \approx 0.75\rho_1 u_s^2$ for $2 < M_s < 4$ for models considered here (see Fig. 5). Hence, for large M_0 the postshock CR pressure can be approximated as $P_{c,2}/\rho_0 u_0'^2 \approx 1 - 0.75(u_s/u_0') - (u_d/u_0')$. Since $u_0' \approx 0.85|u_0|$ and $u_s \approx 0.17|u_0|$ for $M_0 = 30$ shock, $P_{c,2}/\rho_0 u_0'^2 \sim 0.8$, which is consistent with what we found in our simulations.

The CR energy ratio, Φ, increases with time but asymptotes to a constant value once $P_{c,2}$ has reached a quasi-steady value. As mentioned in the previous section, this results from the "self-similar" behavior of the P_c distribution. Since both the numerator and denominator in equation (18) increase approximately linearly with time in the case of the self-similar evolution of E_c, Φ becomes steady

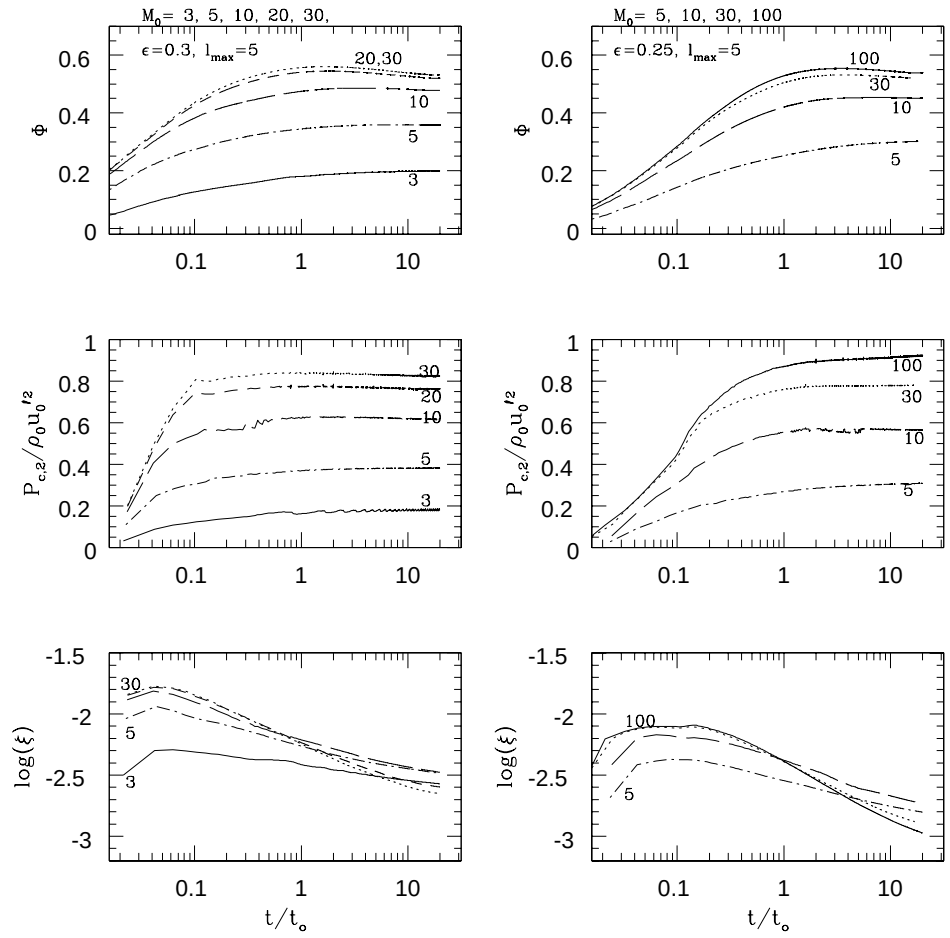

FIG. 6.—Ratio of total CR energy in the simulation box to the kinetic energy in the initial shock rest frame that has entered the simulation box from upstream, $\Phi(t)$, the postshock CR pressure in units of upstream ram pressure in the instantaneous shock frame, and time-averaged injection efficiency $\xi(t)$. Left three panels are for $M_0 = 3$–30 and $\epsilon = 0.3$. Right three panels show the same quantities for $M_0 = 5$–100 and $\epsilon = 0.25$.

when $P_{c,2}$ becomes constant. Time-asymptotic values of Φ increase with the initial Mach number M_0 and $\Phi \approx 0.53$ for $M_0 = 30$ at the terminal time (see also Fig. 12). On the other hand, time asymptotic values of Φ' become $\Phi' \approx \Phi(u_0'/|u_0|)^3 \sim 0.86$ for the $M_0 = 30$ shock model.

The initial injection rate before the weakening of the subshock is roughly independent of M_0 for strong shocks, as we expect from the discussion in § 3.3. Initially it briefly increases to $\xi \sim 0.01$ for strong shocks until $t \sim \tau_{\rm acc}(p_{\rm inj})$, the acceleration timescale of the injection momenta. The initial brief rise in ξ is a numerical artifact occurring in the interval when the initially pure Maxwellian distribution adjusts to form a nonthermal tail in the momentum range where injection takes place. Afterward it decreases as the subshock weakens, since the injection is less efficient at low Mach number shocks. After the initial adjustment period the injection rate decreases as a power-law form with time, $\xi \sim \xi_0 \tilde{t}^{-\alpha}$ for $0.05 < \tilde{t} < 20$, where $0.15 \lesssim \alpha \lesssim 0.4$ with larger values for higher M_0. Although the subshock Mach number decreases to similar values after $\tilde{t} = 0.1$ for all models (see Fig. 5), the injection rate decreases faster for higher M_0 models. This can be explained as follows. The injection momentum $p_{\rm inj}$ after $\tilde{t} = 0.1$ is smaller for higher M_0, since the subshock velocity is reduced further in response to stronger structure modification. Diffusive particle flux upstream, which is realized numerically in our code with a given subshock thickness (Δx_5), is reduced if $D_{\rm diff}(p_{\rm inj}) < \Delta x_5$. The resulting injection rate is smaller for higher M_0 models in which the injection momentum is lower. Thus, the strong decrease of ξ for high M_0 models below the level of ξ for $M_0 = 3$ model should be regarded as a numerical artifact due to a fixed shock thickness.

In order to explore the dependence of our injection model on the parameter ϵ, we also considered the same shock models with $\epsilon = 0.25$ and show Φ, $P_{c,2}$, and ξ in the right three panels of Figure 6. Because of less efficient injection compared to $\epsilon = 0.3$ cases, the initial increases of $P_{c,2}$ and Φ are delayed somewhat, and their time-asymptotic values are reduced a little, as well. Before $\tilde{t} \sim 1$, the CR pressure is dominated by nonrelativistic particles, and the details of the injection history are important to the shock structures. Afterward, the relativistic particles dominate, and the results become less sensitive to the values of ϵ and the details of the injection process. For example, the injection rate ξ is 2–3 times lower with $\epsilon = 0.25$ than with $\epsilon = 0.3$ for the $M_0 = 30$ shock, but the time-asymptotic value of Φ is smaller by only 2%. In summary, the CR energy ratio, Φ, depends sensitively on M_0 for weak shocks, then becomes independent on M_0 for strong shocks, but depends only weakly on the injection rate (ϵ).

5.1.3. *The Particle Distribution*

Time evolution of the distribution function $g(p) = f(p)p^4$ *at the shock* is shown in Figure 7 ($M_0 = 5$) and Figure 8 ($M_0 = 30$) along with the changes in the transparency function $\tau_{\rm esc}$. The Maxwellian distribution shifts to lower momenta primarily because of weakening of the gas subshock in response to flow deceleration in the precursor but also because of the loss of thermal energy to the injection process. As the subshock weakens the postshock flow speed in the subshock rest frame, u_d, decreases, so the transparency function also shifts to lower momenta. As shown in Figure 1, the ratio of $v_{\rm inj}/v_{\rm th}$ increases as the subshock weakens, leading to decreases in the injection rate. For momenta just above the injection pool, the distribution function changes smoothly from a Maxwellian distribution to an approximate power law whose index is close to the test-particle slope for the subshock. However, we note that the particle distribution at lower energy does not evolve as a simple power law, but, instead, it depends on the time-dependent injection history, since the subshock properties and $\tau_{\rm esc}(u_d)$ vary with time and their numerical solutions in our simulations contain low-amplitude noise. Those "historical details" become smeared out at higher momenta. While a fraction of particles injected earlier continues to be accelerated to higher momenta so that $p_{\rm max}(t)$ increases, the amplitude of $g(p)$ at the shock and at a given momentum decreases with time for $p < p_{\rm max}(t)$ due to diffusion.

These results can be compared with those of Gieseler et al. (2000), in which a hydrodynamic code based on the total variation diminishing (TVD) scheme was used. In Gieseler et al. (2000) the diffusion coefficient was 100 times larger than the value used in the present study, so in a comparison the length and timescales should be scaled by that amount. The main difference between the current CR/AMR code and the CR/TVD code is that the subshock is maintained as a discontinuous jump in the CR/AMR code. Numerical gradients defined at the subshock therefore span a single regular zone. Given the same nominal spatial resolution, the shock is more sharply resolved in the CR/AMR simulations. This affects the diffusion of suprathermal particles near the shock and so leads to higher injection rate.

5.2. *Models with* $\epsilon = 0.17$–0.2

In order to extend the calculation to much longer simulation times so that much more energetic particles will be accelerated, we need to include a larger computational domain because of the fast spatial diffusion of the highest energy particles. Thus, the computational time for such calculations becomes very demanding. We increase the refinement level to $l_{\rm max} = 7$ and consider a computation domain

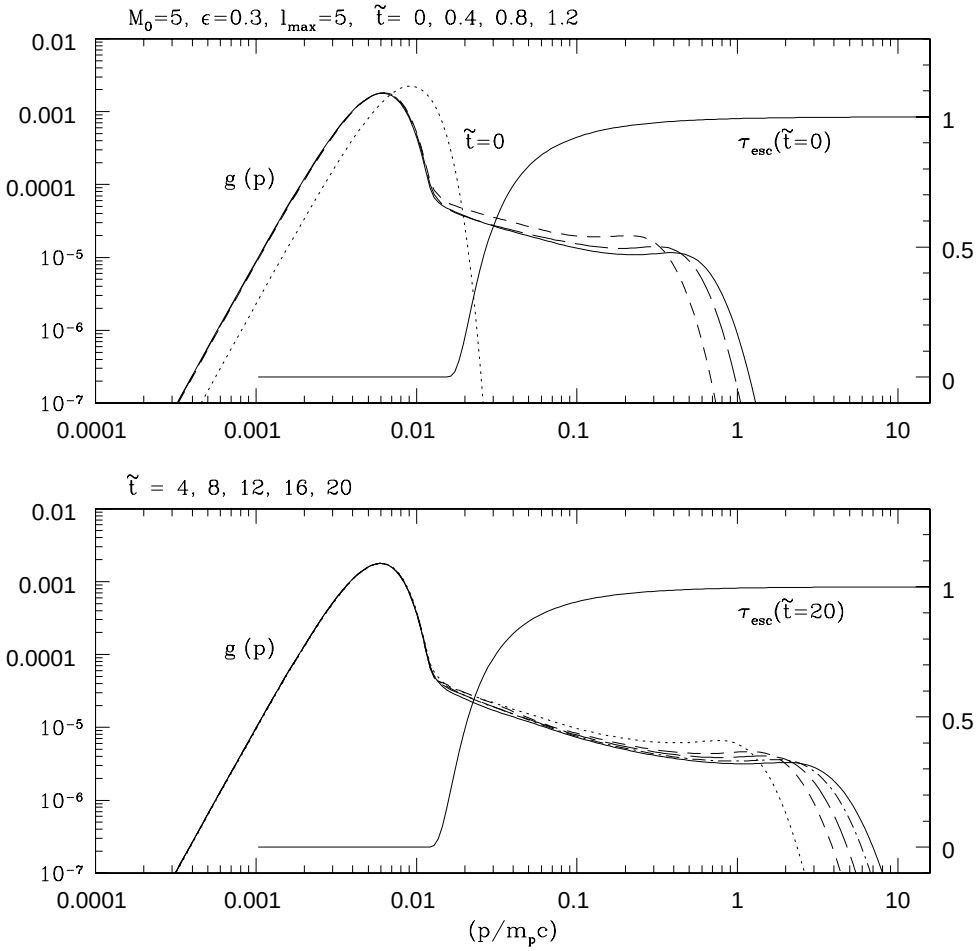

FIG. 7.—Evolution of the CR distribution function at the shock, represented as $g = p^4 f(p)$, shown for the same shock as in Fig. 3 ($M_0 = 5$ and $\epsilon = 0.3$). The transparency function is also plotted at $t/t_0 = 0$ and 20 for reference. The axis on the left side is for $\log g$, while the axis on the right side is for $\tau_{\rm esc}$.

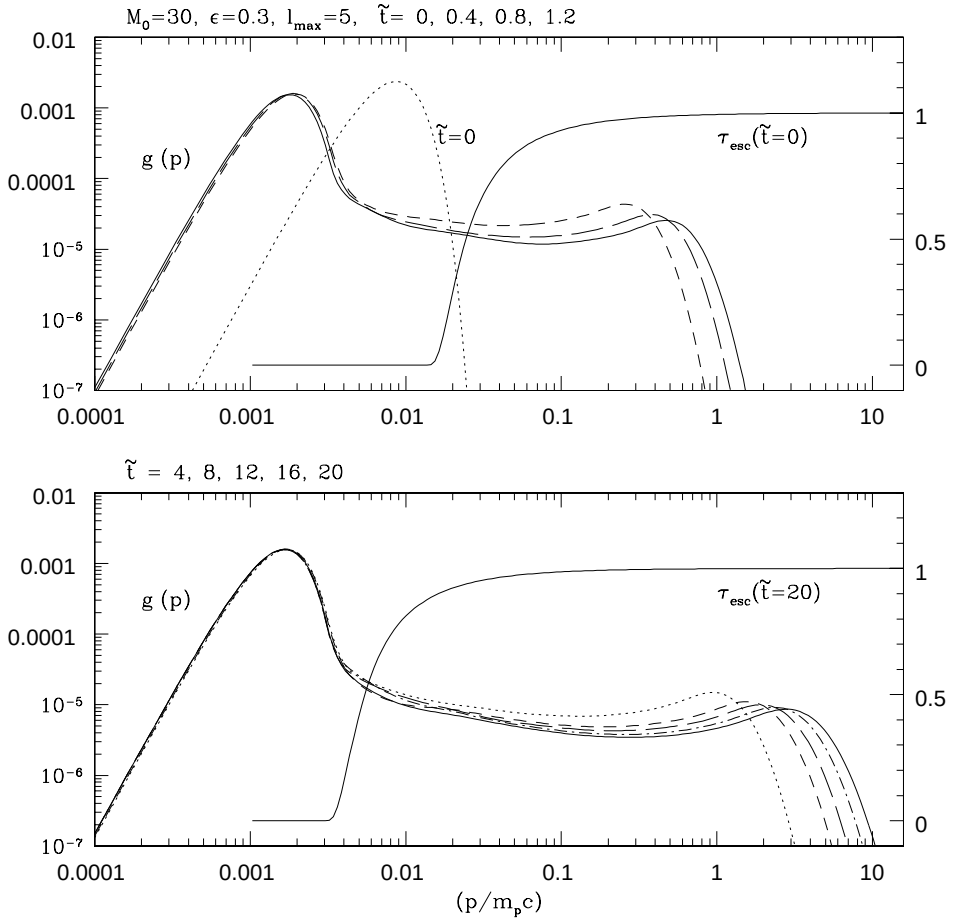

FIG. 8.—Evolution of the CR distribution function at the shock, represented as $g = p^4 f(p)$, shown for the same shock in Fig. 4 ($M_0 = 30$ and $\epsilon = 0.3$). The transparency function is also plotted at $t/t_0 = 0$ and 20 for reference. The axis on the left side is for $\log(g)$, while the axis on the right side is for $\tau_{\rm esc}$.

10 times larger than that of the stronger injection calculations discussed in § 5.1. This forces us to choose smaller values of $\epsilon = 0.17$–0.2 (weaker injection rate) to avoid the initialization numerical problem mentioned in § 4.3. For $M_0 = 5$–100 $\epsilon = 0.2$ is used, while for $M_0 = 150$ and 200 $\epsilon = 0.17$ is used for $\tilde{t} \le 1$, then increased to $\epsilon = 0.2$ for $\tilde{t} > 1$.

5.2.1. *Shock Structure Modification*

Figure 9 shows the evolution of the shock structure for a $M_0 = 200$ shock at much later times up to $\tilde{t} = 140$. Overall shock structures reach *approximate* time-asymptotic states after the initial quick adjustment and then follow "self-similar" evolutions afterward, as in the the $M_0 = 30$ shock with $\epsilon = 0.3$ shown in Figure 4. The subshock slows down and drifts with the velocity $u_{\rm drift} \approx -0.025$ after the shock structure evolution became quasi-steady for the strong shock models, and the starting velocity shift relative to the initial shock rest frame was $u_{\rm shift} = 0.145$. So the time-asymptotic velocity of the subshock relative to far upstream becomes $u_0' \approx 0.83$ for $\epsilon = 0.2$ for strong shocks (see also Fig. 12). This shock speed was $u_0' \approx 0.85$ for $M_0 = 30$ shock model with $\epsilon = 0.3$. The subshock Mach number decreases with time but reaches quasi-steady values after $\tilde{t} = 100$. The values of M_s at $\tilde{t} = 100$ seem to scale with the initial shock Mach number M_0 roughly as $M_s \sim 2.9 M_0^{0.13}$. Although the postshock CR pressure and the subshock speed become roughly quasi-steady after the initial fast modification stage, the precursor compression continues to increase up to the terminal time, and the rate of this increase is higher for higher M_0 models. We see that γ_c is the largest near the shock where the injected suprathermal particles are dominant. But it becomes smaller away from the shock, because relativistic particles dominates there. The spatial distribution of P_c peaks sharply from upstream at the subshock on account of the small diffusion length scale reflecting the dominance of low-energy particles near the subshock.

5.2.2. *Injection and Acceleration Efficiencies*

The evolution of Φ, $P_{c,2}$, and ξ for $M_0 = 5$–200 with $\epsilon = 0.2$ is shown in the left three panels of Figure 10. Note again that we set $\epsilon = 0.17$ when $\tilde{t} \le 1$ and $\epsilon = 0.2$ when $\tilde{t} > 1$ for $M_0 = 150$ and 200 in order to avoid the initial convergence failure of the Riemann solver. So the injection is slower in these two models, resulting in a retarded evolution of all related quantities until $\tilde{t} > 1$. In the evolved shocks the CR pressure at the subshock is higher for larger values of M_0 and becomes $P_{c,2} \approx 0.9 \rho_0 u_0'^2$ for $M_0 \gtrsim 50$. For high initial Mach number shocks ($M_0 \gtrsim 50$) the CR energy ratio approaches $\Phi \approx 0.6$, resulting in $\Phi' \approx \Phi(|u_0|/u_0')^3 \approx 1$, since the approximate time-asymptotic value of $u_0'/|u_0|$ is 0.83 for strong shocks. This high efficiency is possible because CRs

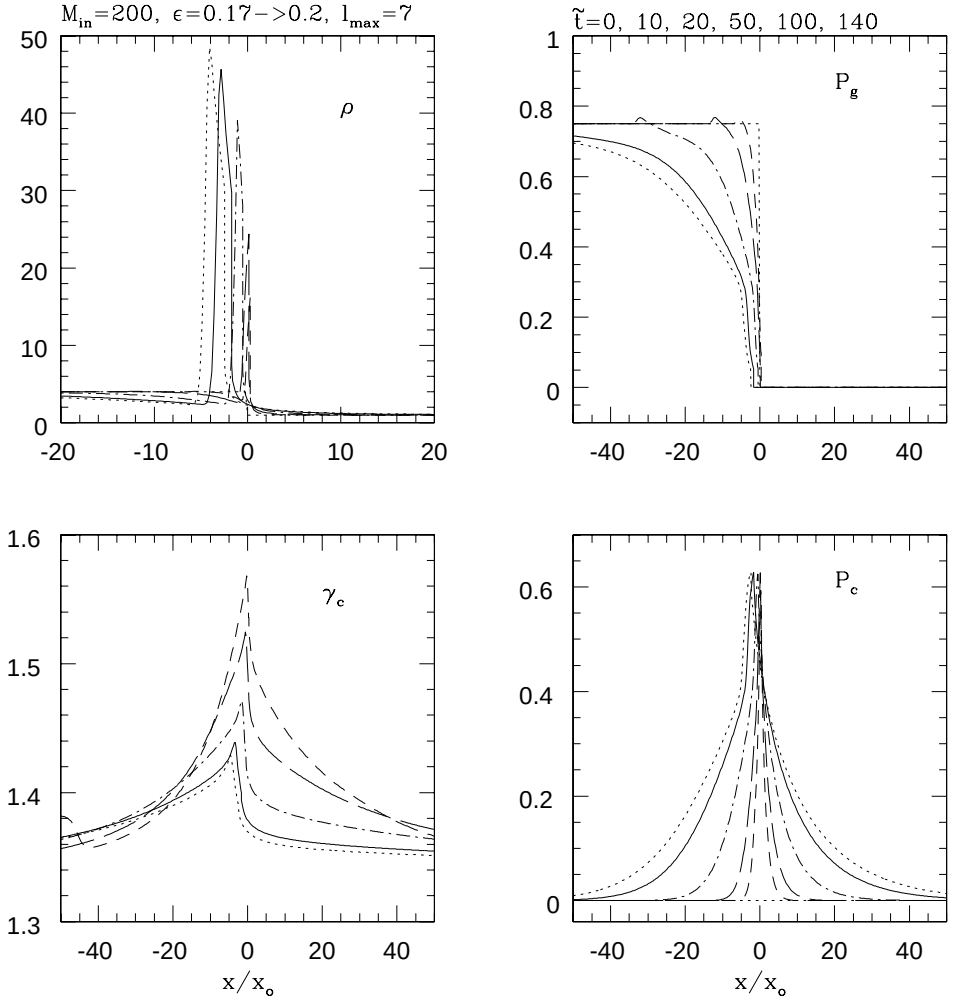

FIG. 9.—Gas density, pressure, CR adiabatic index, and CR pressure shown at $t/t_0 = 0$, 10, 20, 50, 100, and 140 for a $M_0 = 200$ shock. The maximum level of refinement was $l_{\max} = 7$. The shock drifts to the left, so the rightmost transitions correspond to the earliest time $t = 0$.

have absorbed some of the thermal and kinetic energy from the initial shock structure inside the simulation box, in addition to the kinetic energy that has entered the shock during the simulation, $\int 0.5\rho_0 u_0^3\, dt$. We note that the "undulating" features in the time evolution of $P_{c,2}$ seem to be numerical artifacts and not real. Unlike other spatially averaged or integrated quantities, the plotted $P_{c,2}$ is sampled exactly at the subshock (i.e., from one zone) whose properties show small, noisy variations in time. These features seem in particular to correspond to times when the subshock crosses a regular zone boundary and are most prominent for the injection models with $\epsilon = 0.17$–0.2.

Once again the initial injection rate before the weakening of the subshock is independent of M_0 for strong shocks, and it is about 4 times smaller than that of $\epsilon = 0.25$ models and about 8 times smaller than that of $\epsilon = 0.3$ models. For $1 < \tilde{t} < 200$, the time-averaged injection rate can be fitted as a power law, $\xi \sim 2.5 \times 10^{-3}\tilde{t}^{-0.4}$, for strong Mach shocks. As discussed in § 5.1.2, the injection rate decreases with time mainly because the subshock weakens due to CR modification but partly because the diffusive flux of injected particles crossing the shock decreases for smaller injection momentum. If the effective numerical subshock thickness (spatial resolution) were set up to decrease as the postshock temperature decreased, we expect the injection rate for high M_0 shocks would level off to the level similar to that for low M_0 shocks, that is, $\xi \sim 10^{-3.4}$ found for the $M_0 = 5$ case. Below we will list this for our estimated asymptotic rate. Considering the lack of our understanding of the detail physics of the shock transition, this should be considered a rough estimate.

The same set of quantities are shown in the right three panels of Figure 10 for $M_0 = 30$ for $\epsilon = 0.2$, 0.23, and 0.25, in order to study the effects of different injection rates. Obviously larger values of ϵ (i.e., more leakage) lead to higher injection rate, ξ, and so acceleration of CRs proceeds faster. For all values of ϵ considered, however, time-asymptotic values of $P_{c,2}/\rho_0(u_0 t)^2 \sim 0.8$ and $\Phi \sim 0.6$, even though the injection histories are different. This implies that the long-term behavior of Φ is mostly dependent on the initial shock Mach number but only weakly dependent on the details of the injection rate, so long as it is in the range seen here. If the injection rate falls below some critical range, other studies have emphasized that shock modification can be minimal so that "test particle" solutions apply (e.g., Berezhko et al. 1995; Malkov, Diamond, & Völk 2000). It seems mostly likely that all the shocks simulated here will remain strongly modified, corresponding to "high injection efficiency," although we cannot yet judge if they would eventually approach some kind of self-organized critical condition

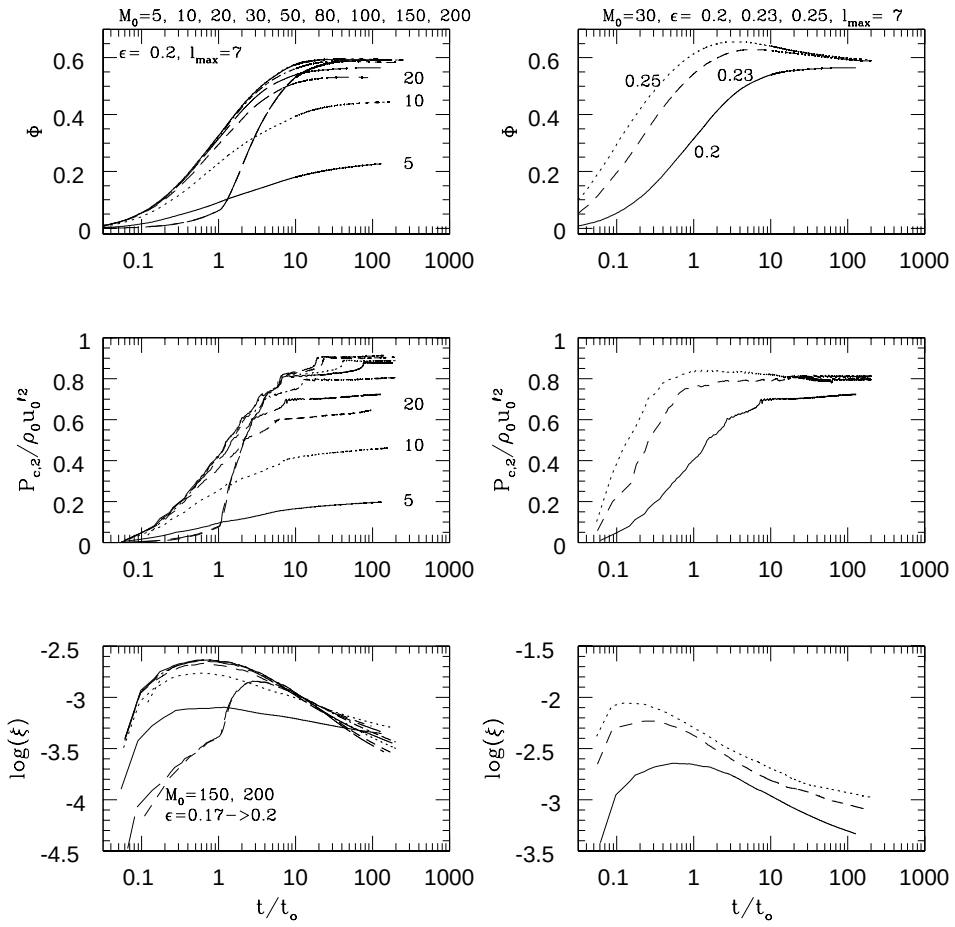

FIG. 10.—Ratio of total CR energy in the simulation box to the kinetic energy in the initial shock rest frame that has entered the simulation box from upstream, $\Phi(t)$, the postshock CR pressure in units of upstream ram pressure in the instantaneous shock frame, and time-averaged injection efficiency, $\xi(t)$. Left three panels are for $M_0 = 5$–200 and $\epsilon = 0.2$. Right three panels are for $M_0 = 30$ and $\epsilon = 0.2$, 0.23, and 0.25.

such as that suggested by Malkov et al. (2000). Evaluating that possible eventuality will likely require self-consistent treatments of the coupling between evolution of CRs and the diffusion coefficient. That is beyond the scope of the present work.

5.2.3. *The Particle Distribution*

The evolution of the CR distribution function for a $M_0 = 100$ shock is shown in Figure 11. The general behavior is the same as the early evolution for the $M_0 = 30$ shock with $\epsilon = 0.3$ shown in Figure 8. In particular, both the thermal distribution and the transparency function shift to lower momenta, the function $g(p)$ shows the characteristic "concave upward" curves reflecting modified shock structure. The CR spectrum extends to higher momenta with time, but the amplitude at intermediate momenta decreases with time. The slope of the CR spectrum, defined as $q = -(\partial \ln f/\partial \ln p)$, ranges over $4.1 \lesssim q \lesssim 4.4$ near $p_{\rm inj}$, reflecting $r_{\rm sub} \gtrsim 3$ then decreases with the particle momentum and converges for strong shocks to $q \sim 3.1$ just below $p_{\rm max}$.

5.3. *Time Asymptotic Behaviors*

Although our CRASH code is much more efficient than conventional codes used for this problem, we have thus far integrated our models only until the maximum momentum reaches about $\sim 40 m_p c$ ($\tilde{t} = 200$), since computational requirements of using a Bohm type diffusion model are still substantial. However, some characteristics of the shock seem to have reached quasi-steady states well before the end times of our simulations. So we can make an attempt to project the long-term, time-asymptotic behaviors of these CR-modified shocks from our results. For strong shocks of $M_0 \gtrsim 30$, the CR injection via thermal leakage is very efficient, and so the CR pressure quickly dominates over the gas pressure. The postshock CR pressure reaches approximate time-asymptotic values by the time the injection and acceleration become balanced by the advection and diffusion of CRs away from the shocks. As compression increases through the precursor, the subshock slows down, and the subshock velocity relative to the far upstream flow approaches $u_0' \sim (0.83$–$0.85)|u_0|$ for strong shocks with the inverse wave amplitude parameter considered here, $\epsilon = 0.2$–0.3. As a result, the postshock CR pressure asymptotes to a quasi-steady value of $P_{c,2} \sim 0.9\rho_0 u_0'^2 \sim 0.63\rho_0 u_0^2$ for strong shocks. Approximate estimates for time-asymptotic values of the CR energy ratio Φ are calculated at $\tilde{t} = 20$ for models with $\epsilon = 0.3$ and 0.25, and at $\tilde{t} = 100$ for models with $\epsilon = 0.2$. They are plotted as a function of the initial shock Mach number M_0 in the right top panel of Figure 12. Also time-asymptotic values of $u_0'/|u_0| = M_0'/M_0$ are calcu-

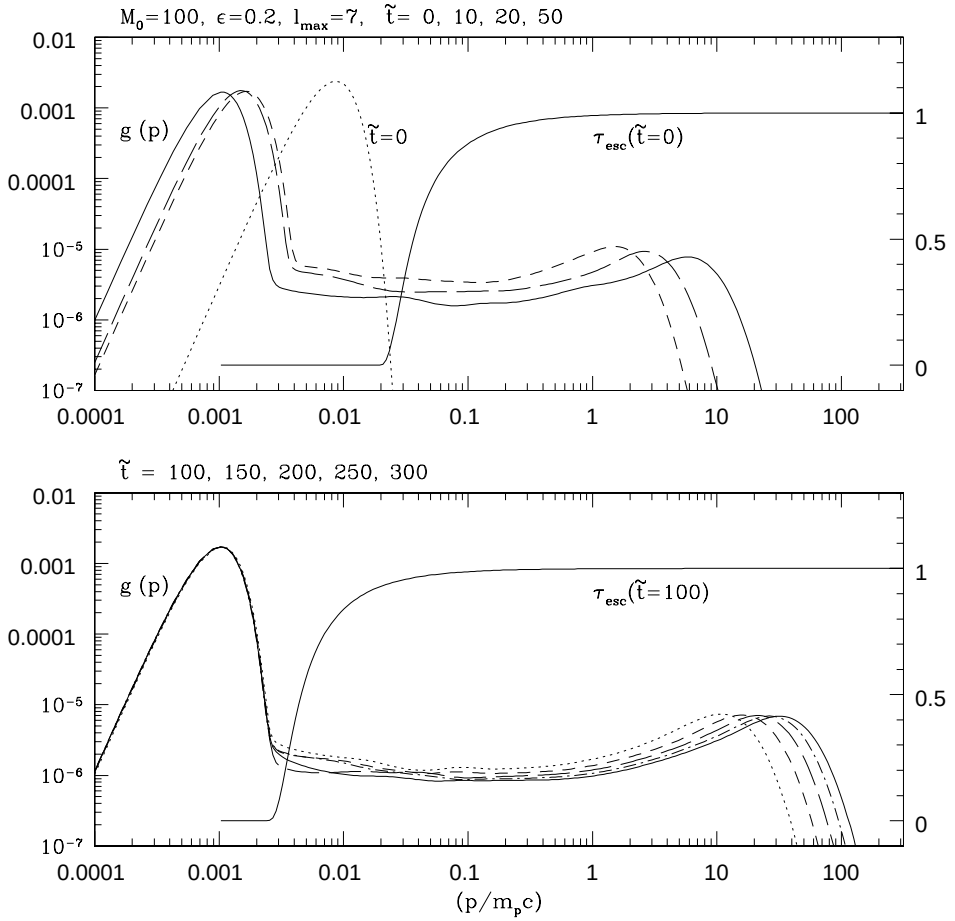

FIG. 11.—Evolution of the CR distribution function at the shock, represented as $g = p^4 f(p)$, shown for the $M_0 = 100$ shock with $\epsilon = 0.2$. The transparency function is also plotted at $t/t_0 = 0$ and 100 for reference. The axis on the left side is for $\log(g)$, while the axis on the right side is for $\tau_{\rm esc}$.

lated at $\tilde{t} = 100$ for models with $\epsilon = 0.2$ and shown in the right middle panel of Figure 12. We can estimate time asymptotic values of Φ' as $\Phi(|u_0|/u_0')^3$ using data in these two plots. We also show time-asymptotic values of the CR pressure at the shock normalized to the ram pressure of the initial shock, $P_{c,2}/\rho_0 u_0^2$ (*solid line*), and that normalized by the ram pressure of the instantaneous shock, $P_{c,2}/\rho_0 u_0'^2$ (*dotted line*), which are calculated at $\tilde{t} = 100$ for $\epsilon = 0.2$ shocks in the right bottom panel of Figure 12.

Some other characteristics of the subshock, on the other hand, show slow secular changes, even after the postshock P_c becomes quasi-steady. As the CR distribution continues to harden, for example, the effective adiabatic index of the flow decreases with time. Also the precursor spreads farther out, the compression through the precursor increases, and the subshock continues to weaken. The entire shock structure broadens linearly with time in a "self-similar" way, because of the strongly momentum-dependent diffusion matching the advective spreading behind the shock. As a result, unless we enforce an escaping upper momentum boundary [i.e., $g(p) = 0$ for $p > p_1$, where p_1 is the upper momentum boundary], the CR-modified shock would not reach a strict steady state.

According to kinetic equation simulations of spherical blast waves (Berezhko et al. 1995; Drury et al. 1995), and both Monte Carlo and kinetic equation calculations of steady planar shocks with strongly momentum-dependent diffusion (Malkov 1997; Berezhko & Ellison 1999), a CR-modified shock characteristically retains a subshock with the compression ratio $2.5 < r_{\rm sub} < 4$ and does not become a completely smooth transition. In the present time-dependent planar shock simulations with Bohm-like diffusion we also found that the subshock remains. The values for the subshock Mach numbers in our shocks can be described by the scaling $M_s \sim 2.9 M_0^{0.13}$ at the end of the simulations. Since the subshock compression ratio is related to the gas subshock Mach number as $r_{\rm sub} = 4/(1 + 3/M_s^2)$, this leads to $2.5 < r_{\rm sub} < 4$. Steady, adiabatic compression through the precursor can be expressed simply as $\rho_1/\rho_0 = (M_0'/M_s)^{(\gamma_g+1)/2}$, where $M_0' = M_0(u_0'/u_0)$ is the time asymptotic value of the shock Mach number with respect to the far upstream flow. Then the total compression ratio $r_{\rm tot} = \rho_2/\rho_0$ for a *steady* CR-modified shock with a subshock can be expressed in terms of the subshock Mach number and the subshock compression ratio as

$$r_{\rm tot} = r_{\rm sub}(M_0'/M_s)^{3/4} \tag{22}$$

(Berezhko & Ellison 1999). Here $r_{\rm sub} M_s^{-3/4} = 4M_s^{5/4}/(M_s^2 + 3)$ from the shock jump condition. So $r_{\rm sub} M_s^{-3/4} = 0.96$–$1.36$ for the subshock Mach numbers found in our simulations (i.e., $2 \le M_s \le 6$). Both Berezhko et al. (1995) and Berezhko & Ellison (1999) found that $r_{\rm sub} M_s^{-3/4} \sim 1$ for total Mach numbers (M_0') considered so

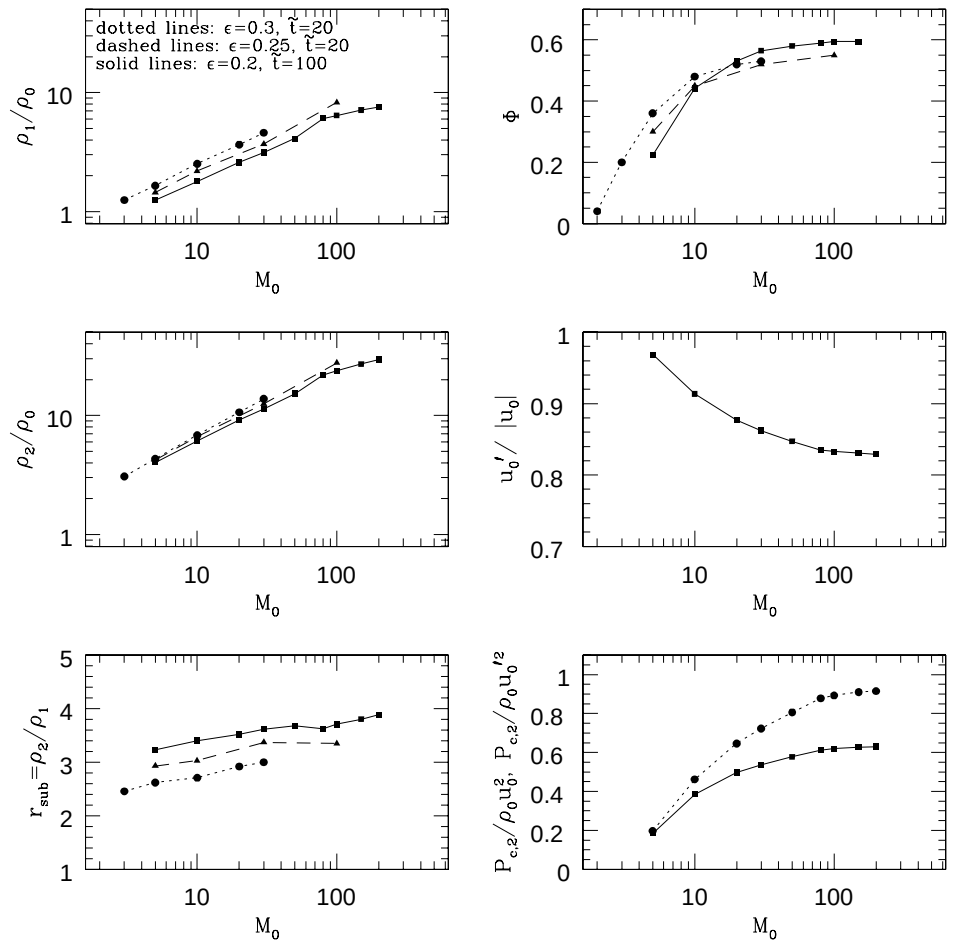

FIG. 12.—*Left three panels*: preshock density, ρ_1/ρ_0, postshock density, ρ_2/ρ_0, and subshock compression ratio for $M_0 = 5$–200. For models with $\epsilon = 0.3$ and 0.25 the numerical results at $\tilde{t} = 20$ are plotted, while for models with $\epsilon = 0.2$ the results at $\tilde{t} = 100$ are plotted. *Right top panel*: approximate time asymptotic values of Φ is plotted. The same symbols and line types are used as in ρ_1/ρ_0 plot. *Right middle panel*: time asymptotic values of the upstream flow velocity relative to the subshock, u_0', at $\tilde{t} = 100$ are plotted for $\epsilon = 0.2$. *Right bottom panel*: time asymptotic postshock CR pressure normalized to the ram pressure of the upstream flow in the initial shock rest frame, $P_{c,2}/\rho_0 u_0^2$ (*solid line*), and to the ram pressure of the upstream flow in the instantaneous shock rest frame, $P_{c,2}/\rho_0 u_0'^2$ (*dotted line*), is plotted for $\epsilon = 0.2$.

that the total compression ratio scales with the total Mach number as $r_{\rm tot} \sim (M_0')^{3/4}$. For comparison we plotted in the left three panels of Figure 12 the preshock (ρ_1/ρ_0), postshock (ρ_2/ρ_0) densities, and subshock compression factor ($r_{\rm sub}$) at $\tilde{t} = 20$ for models with $\epsilon = 0.3$ and 0.25, and at $\tilde{t} = 100$ for models with $\epsilon = 0.2$ as a function of the initial shock Mach number M_0. We note once again that the precursor compression continues, although very slowly, so these quantities have not reached time-asymptotic values at the terminal time of our simulations. For our simulated shocks with $\epsilon = 0.2$ the ratio ρ_2/ρ_0 shown in Figure 12 can be approximated by a power law, $\rho_2/\rho_0 \sim 1.5 M_0^{0.6}$ for $M_0 < 80$. But this power-law relation flattens out for $M_0 > 80$. Considering that ρ_2 has not reached a quasi-steady value at $\tilde{t} = 20$ or $\tilde{t} = 100$, especially for high Mach number shocks, and that the ratio M_o'/M_0 decreases with M_0, our empirical relation for $r_{\rm tot}$ versus M_0' is likely to steepen if we run the simulations for much longer times. As discussed in § 5.1.1, the scaling relation for the compression ratio results simply from the fact that the subshock persists in our simulated shocks, which broadens in space self-similarly with time due to strongly momentum-dependent diffusivity, but are not yet stationary. According to Malkov (1997), the total compression saturates at the level of $(\nu p_{\rm max}/p_{\rm inj})$ for $M_0' > (\nu p_{\rm max}/p_{\rm inj})^{4/3}$, where ν is his injection parameter. For strong shocks in our simulations, $\nu \sim 4 \times 10^{-2}$ and $p_{\rm max}/p_{\rm inj} \sim 2 \times 10^4$, so the shocks considered here are not in the saturation limit.

6. SUMMARY

In order to study cosmic-ray modified shocks we have developed a new numerical code, CRASH (Cosmic-Ray Amr SHock), by implementing a thermal leakage injection scheme introduced by Gieseler et al. (2000) into a new hydro/CR code with adaptive mesh refinement and shock tracking scheme by Kang et al. (2001). Our CR injection model is based on the "thermal leakage" process at quasi-parallel CR shocks. Injection is regulated by the convolution of the population in the high-energy tail of the Maxwellian velocity distribution of the postshock gas and a transparency function, $\tau_{\rm esc}(p, u_d, \epsilon)$, determined by the strength of downstream MHD waves, expressed by a parameter, ϵ. The injection rate in our model is then controlled largely by the subshock Mach number M_s, since that determines the ratio of the postshock flow speed to the

breadth of the thermal distribution. For weak shocks, injection becomes more difficult as M_s decreases but is independent of M_s for strong shocks, when the subshock compression asymptotes. With our CRASH code the CR injection and acceleration at astrophysical shocks can be simulated numerically even for strongly momentum-dependent spatial diffusion coefficients.

Using these tools the time evolution of CR shocks has been followed with a Bohm-type diffusion model. We started from the initial conditions for pure gasdynamic shocks of various initial Mach numbers (M_0) without any preexisting CRs. In such simulations the CR injection rate is not treated as a fixed free parameter, as it has been done traditionally. Instead, once an "intelligent estimate" is made of the strength of the trapping wave field of the downstream MHD turbulence, the injection is followed naturally and self-consistently during nonlinear evolution of the flows. For strong shocks with initial strengths, $M_0 \gtrsim 30$, a substantial portion of the particles in the tail of the Maxwellian distribution have velocities high enough to leak upstream against the wave-particle interactions, so the injection is efficient and fast. As the CR pressure increases at the subshock and the in-flowing plasma is compressed, however, the subshock slows down with respect to the far-upstream flow. This modification occurs rather promptly and before the postshock CR pressure reaches an approximate time-asymptotic value. Afterward the evolution of the shock structure becomes secular. For strong shocks, the subshock speed in our simulations decreases by about 15%–17%, and the postshock CR pressure absorbs up to 60% of the ram pressure of the initial shock, which corresponds to 90% of the ram pressure of the upstream flow in the evolved subshock rest frame at the end of our simulations. Once the postshock CR pressure becomes constant, the shock structure evolves approximately in a "self-similar" way, because the scale length of shock broadening increases linearly with time.

The injection rate, defined as the fraction of the particles passed through the shock that are accelerated to form the CR population, becomes as high as $\xi \sim 0.01$ early in the evolution of strong shocks, independent of M_0. As the shock is modified, however, the subshock Mach number decreases down to $M_s \sim 2.9 M_0^{0.13}$, and the injection rate reduces toward the limiting value corresponding to weak subshocks. Our approximate numerical estimate for the limiting value is $\xi \sim 10^{-3.4}$ for models with $\epsilon = 0.2$. Since the CR spectrum continues to extend to higher momenta, and since those highest energy particles diffuse rapidly away from the shock when $\kappa \propto p$, energy begins to be transported away from the shock transition. This allows the subshock to persist and the total compression to become large compared to steady energy-conserving gasdynamic shocks. Also the shock structure evolves toward the high compression ratios seen in kinetic equation spherical CR shocks and steady state planar shocks with energy escape through spatial or momentum boundaries.

Finally, the main conclusions of our time-dependent simulations of CR-modified shocks based on Bohm-like diffusion and a physically based thermal leakage CR injection are as follows:

1. In the strong shock limit of initial Mach number $M_0 \gtrsim 30$, significant physical processes such as injection and acceleration become largely independent of the initial shock Mach number and only weakly depend on the postshock wave amplitude parameter ϵ for values considered here ($0.2 \leq \epsilon \leq 0.3$). According to our thermal leakage model, the overall injection rate approaches $\xi \sim 10^{-3}$, and the fraction of upstream flow kinetic energy *in the initial shock rest frame* that has been transferred to CRs is $\Phi \sim 0.6$ for strong shocks. The ratio of the postshock CR pressure to the *instantaneous* ram pressure of the subshock with respect to the upstream plasma approaches ~90%. On the other hand, the injection rate and acceleration efficiency are sensitively dependent on M_0 for low Mach number shocks ($M_0 \lesssim 30$).

2. In our simulations, with no initial CRs around the shock, the thermal leakage injection is very efficient initially when the subshock is strong, but it becomes much less efficient as the subshock weakens because of nonlinear feedback from the CR pressure. For example, the time-averaged injection rate can be fitted as a power-law form $\xi \sim 2.5 \times 10^{-3} (\tilde{t})^{-0.4}$ for $1 < \tilde{t} < 200$ ($\tilde{t} = t/t_0$) for strong shocks of $M_0 \gtrsim 30$ and the inverse wave-amplitude parameter $\epsilon = 0.2$.

3. Although some particles injected early in the shock evolution continue to be accelerated to ever higher energies, the immediate postshock CR pressure reaches a quasi-steady value when a balance between injection/acceleration and advection/diffusion is achieved. The region of quasi-steady postshock properties spreads for Bohm diffusion in an almost self-similar fashion because both diffusive and advection rates scale linearly with time. This expansion maintains the large precursor compression at values that can be large compared to what one would derive from Rankine-Hugoniot relations for steady gas shocks with a relativistic equation of state.

4. The sum of the compression through the precursor and across the subshock calculated near the terminal time, $\tilde{t} = 100$, for models with $\epsilon = 0.2$ can be approximated by $\rho_2/\rho_0 \sim 1.5 M_0^{0.6}$ for $M_0 < 80$, but this ρ_2/ρ_0-M_0 relation flattens for $M_0 \geq 80$. Considering that ρ_2 continues to increase until the terminal time, especially for higher Mach number shocks, and that the Mach number of the subshock with respect to the far upstream (M_0') decreases for strong shocks with high initial Mach numbers (M_0), this is probably consistent with the $\rho_2/\rho_0 \propto M_0'^{3/4}$ scaling relation found for steady shocks and for spherical shocks by several authors (Berezhko et al. 1995; Malkov 1997; Berezhko & Ellison 1999). The large density compression is possible in the planar shocks without energy escape from the whole computed system, since the shock structure spreads out far upstream and far downstream, due to strong momentum-dependent diffusivity.

Although our simulations have been carried out only until the highest momentum is $p_{\max} \sim 40 m_p c$ because of severe computational requirements, these simulation results provide useful guidance for long-term evolution of CR-modified shocks. In a future study, we will extend the integration time so that $p_{\max}/m_p c \gg 1$ can be achieved and the free escape at the upper momentum boundary is applied in order to compare the time-dependent simulations with previous studies of steady state shocks (Ellison & Eichler 1984; Malkov 1997; Malkov & Drury 2001).

The authors would like to thank D. Ryu and M. Malkov for helpful discussions. H. K. was supported by Korea Research Foundation Grant (KRF-2000-015-DP0448).

T. W. J. is supported by NSF grant AST-9619438, by NASA grant NAG5-10774, and by the University of Minnesota Supercomputing Institute. The numerical calculations were performed through "The 2nd Supercomputing Application Support Program" of KISTI (Korea Institute of Science and Technology Information).

APPENDIX

DISCUSSION OF TEST CALCULATIONS

The algorithms applied in CRASH are already mostly well documented and well tested. The hydrodynamic scheme, for example, is a member of the well-known Godunov family and was verified by LeVeque & Shyue (1995). Our Crank-Nicholson scheme for solution of the diffusion-convection equation was tested against previous, independent implementations and analytic test particle DSA solutions in Kang & Jones (1991), where we employed the piecewise parabolic method (PPM) hydrodynamics algorithm. Other tests of nonlinear CR shock solutions using several previous hydrodynamic implementations were given for both diffusion-convection (e.g., Kang et al. 1992; Kang & Jones 1995) and two-fluid (e.g., Jones & Kang 1990; Kang & Jones 1995, 1997) models of CR transport. Kang & Jones (1995) using PPM hydrodynamics and Kang & Jones (1997) using TVD magnetohydrodynamics methods, for example, provided comparisons between the CR transport approach applied here with our earlier "thermal leakage" injection model and Monte Carlo, hybrid plasma simulations, and in situ measurements of heliospheric shocks. While the newer injection scheme utilizes a significantly improved physical model to determine which particles are injected at a shock, both the new and the old underlying numerical schemes have much in common, as discussed in Gieseler et al. (2000). More recently, Kang et al. (2001) provided convergence tests of the combined shock tracking, AMR, convection diffusion code upon which CRASH is based, again using our previous thermal leakage injection model.

In order to extend the above test base to CRASH, we present here several comparisons of solutions to results from these earlier works. In particular we have tested CRASH against piston-driven shock problems that were calculated with our PPM/CR code (Jones & Kang 1990; Kang et al. 1992). First, using a two-fluid version of our CRASH code with the modified entropy equation, we calculated a shock driven by a constant speed, plane piston with $u_p = 0.3$ moving into a medium of $\rho = 1$, $P_g = 7 \times 10^{-4}$, and $P_c = 3.5 \times 10^{-4}$. Closure parameters are assumed to be $\gamma_c = 5/3$ and $\langle \kappa \rangle = 0.01$. There is no injection of new CRs in this case, only reacceleration of the previous CR population. Thus, it is a test for nonlinear modified shocks of the dynamical coupling terms included in equations (2)–(3). Figure 13 shows the evolution of the shock at $t = 3,\ 6$, and 9,

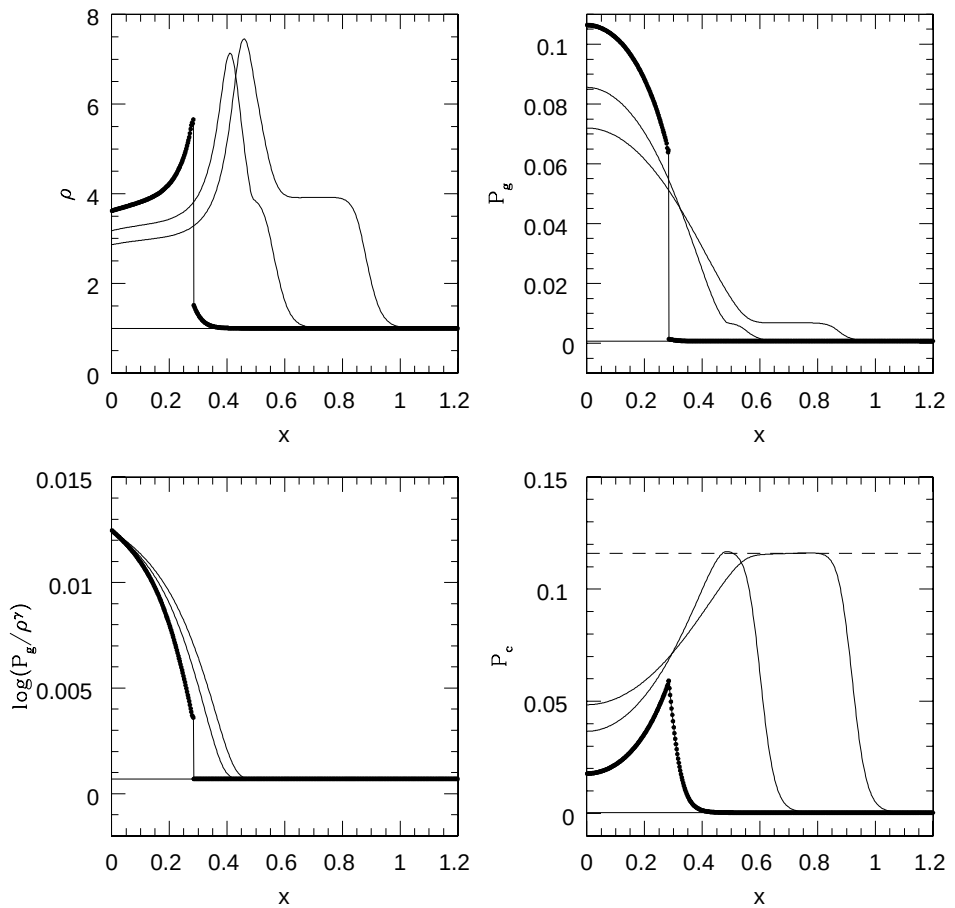

FIG. 13.—Piston-driven shock with $u_p = 0.3$, propagating into a uniform medium of $\rho = 1$, $P_g = 7 \times 10^{-4}$, $P_c = 3.5 \times 10^{-4}$, $\gamma_c = 5/3$, and $\langle \kappa \rangle = 0.01$. CR energy injection at the subshock is not included. The simulation was calculated with the two-fluid version of our CRASH code with the modified entropy (S) equation. The results are shown at $t = 3,\ 6$, and 9. The dashed line corresponds to the postshock P_c in the steady state limit.

which can be compared with Figure 1 of Jones & Kang (1990). Agreement is excellent. The dashed horizontal line shows the steady state solution for P_c, which is fully consistent with the CRASH simulation. This test calculation demonstrates that the two fluid version of the CRASH code can accurately follow the evolution of a strongly CR-modified shock. The dynamical coupling between the CRs and the gas is the same in the two-fluid model as in the diffusion-convection, kinetic equation model, except for the multiscale character introduced by a momentum-dependent diffusion coefficient into the kinetic equation model.

To extend the dynamical evaluation to include momentum-dependent influences, we calculated another piston-driven shock using the diffusion-convection version of CRASH. In this case the piston has velocity $u_p = 1$ moving into a medium of $\rho = 1$, $P_g = P_c = 0.001$. Two simulations were done, one with and one without the modified entropy equation (5). The injection process was turned off, and only the base-grid was used (i.e., $l_{g,\max} = 0$). The diffusion coefficient was given the form $\kappa = p^{0.5}$. Figure 14 shows the evolution of the shock at $t = 10,\ 30,\ 50,\ 100$, and 150, which was calculated with the modified entropy equation. The last of these compares directly with the dotted curves in Figure 3 of Kang et al. (1992). Some details of the early evolution differ, which cause the exact locations and peaks of the transient density spike to differ somewhat, but the overall structures and the shock transitions at $t = 150$ are in very good agreement, including the compression, as well as the gas and CR pressures. The noted small early evolution differences among different codes have been seen before. They reflect the sensitivity to numerical details of the very rapid changes taking place in the shocks at the start of such simulations.

Finally, we demonstrate the benefits of including the modified entropy equation in treatments of strongly modified CR shocks. Figure 15 shows from two simulations the subshocks and precursor structure for the piston-driven shock shown in Figure 14 at $t = 20$. The two sets of curves were calculated with the modified entropy condition enforced (S code: *solid line*) and without it (E code: *dashed line*). The lower left panel shows the specific entropy, $\log P_g/\rho^{\gamma}$. To the right of the subshock, where the flow is adiabatic, this quantity should be a constant. However, because the flow there is highly supersonic, the total energy is dominated by the kinetic energy. Consequently, errors in computing the gas pressures used in equations (2) and (3), as extracted from a combination of the total energy and momentum quantities, lead to significant errors in the entropy of the preshock gas. That, in turn, leads to errors in the gas subshock and CR acceleration behaviors. Enforcing entropy conservation in smooth flows eliminates the problem, as illustrated in the figure.

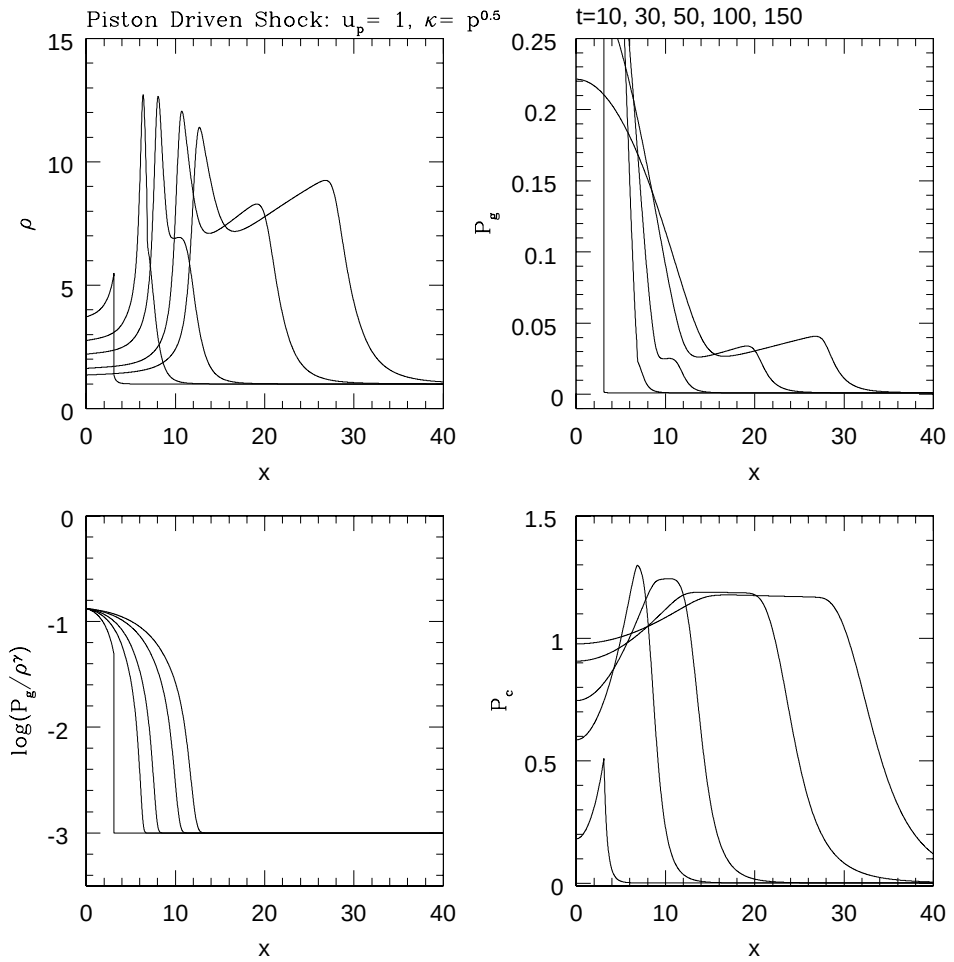

FIG. 14.—Piston-driven shock with $u_p = 1$, propagating into a uniform medium of $\rho = 1$, $P_g = P_c = 0.001$, and $\kappa = p^{0.5}$. CR particle injection at the subshock was turned off. The simulation was calculated with the kinetic version of our CRASH code with the modified entropy (S) equation. The results are shown at $t = 10,\ 30,\ 50,\ 100$, and 150.

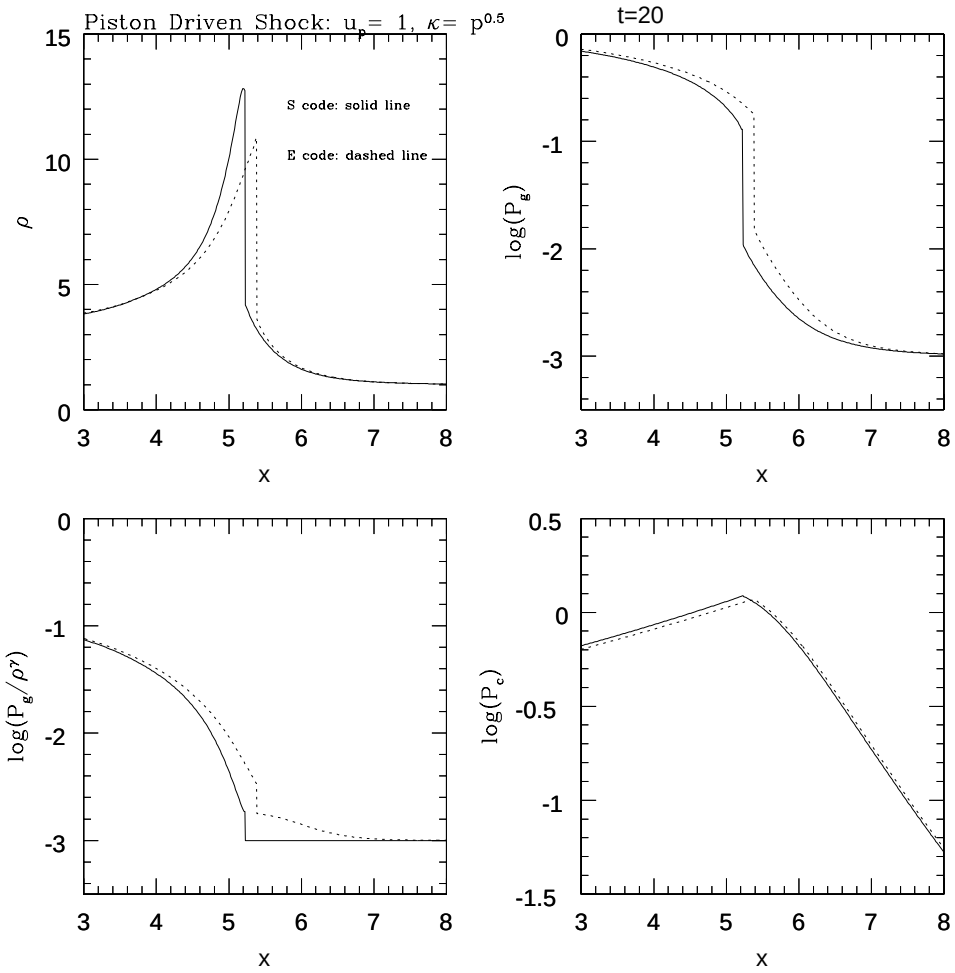

FIG. 15.—Same shock shown as in Fig. 14, but at $t = 20$. The solid lines are for the simulation with the modified entropy equation, while the dashed lines are for the simulation with the total energy equation only.

REFERENCES

Bell, A. R. 1978, MNRAS, 182, 147
Berezhko, E. G., & Ellison, D. C. 1999, ApJ, 526, 385
Berezhko, E. G., & Krymskii, G. F. 1988, Soviet Phys. Uspekhi, 31, 27
Berezhko, E. G., Ksenofontov, L., & Yelshin, V. 1995, Nucl. Phys. B, 39, 171
Berger, J. S., & LeVeque, R. J. 1998, SIAM J. Numer. Anal., 35, 2298
Blandford, R. D., & Eichler, D. 1987, Phys. Rep., 154, 1
Drury, L. 1983, Rep. Prog. Phys., 46, 973
Drury, L., & Falle, S. A. E. G. 1986, MNRAS, 223, 353
Drury, L., Völk, H. J., & Berezhko, E. C. 1995, A&A, 299, 222
Ellison, D. C., & Eichler, D. 1984, ApJ, 286, 691
Gieseler, U. D. J., Jones, T. W., & Kang, H. 2000, A&A, 364, 911
Jones, T. W., & Kang, H. 1990, ApJ, 363, 499
Kang, H., & Jones, T. W. 1991, MNRAS, 249, 439
———. 1995, ApJ, 447, 944
Kang, H., & Jones, T. W. 1997, ApJ, 476, 875
Kang, H., Jones, T. W., LeVeque, R. J., & Shyue, K. M. 2001, ApJ, 550, 737
Kang, H., Jones, T. W., & Ryu, D. 1992, ApJ, 385, 193
LeVeque, R. J., & Shyue, K. M. 1995, SIAM J. Sci. Stat. Comput., 16, 348
Malkov, M. A. 1997, ApJ, 485, 638
———. 1998, Phys. Rev. E, 58, 4911
Malkov, M. A., Diamond, P. H., & Völk, H. J. 2000, ApJ, 533, L171
Malkov, M. A., & Drury, L. 2001, Rep. Prog. Phys., 64, 429
Malkov, M. A., & Völk, H. J. 1995, A&A, 300, 605
———. 1998, Adv. Space Res., 21, 551
Quest, K. B. 1988, J. Geophys. Res., 93, 9649
Ryu, D., Ostriker, J. P., Kang, H., & Cen, R. 1993, ApJ, 414, 1
Skilling, J. 1975, MNRAS, 172, 557